RADIO SCIENCE, VOL. 37, NO. 4, 1048, 10.1029/2000RS002508, 2002

An investigation into the geometric optics approximation for indoor scenarios with a discussion on pseudolateral waves

Michael G. Cotton

Institute for Telecommunication Sciences, National Telecommunications and Information Administration, U.S. Department of Commerce, Boulder, Colorado, USA

Edward F. Kuester

Department of Electrical and Computer Engineering, University of Colorado, Boulder, Colorado, USA

Christopher L. Holloway

National Institute of Standards and Technology, U.S. Department of Commerce, Boulder, Colorado, USA

Received 12 June 2000; revised 22 January 2002; accepted 25 January 2002; published 9 July 2002.

[1] In this study we investigated the geometric optics (GO) approximation to the fields of an infinitesimal electric dipole above a half plane for geometries typical of wireless indoor communications. This inspection was motivated by efforts to establish a ray trace model to characterize indoor radio propagation channels. Eight canonical geometries were examined to isolate near-surface and near-field effects that are not accounted for in the GO approximation. Common building materials and physical dimensions (i.e., antenna separation and height) as small as 1 cm were investigated for frequencies up to 8 GHz. Theoretical fields were calculated via numerical evaluation of Sommerfeld integrals and compared to corresponding GO approximations. As expected, near-field and near-surface (e.g., surface wave) mechanisms which invalidate GO were observed. Close to the surface, an interesting interference pattern in the frequency domain was identified. Mathematical manipulation showed that this so-called "pseudolateral wave" phenomenon was caused by adjacent fields in the two media propagating at different speeds. Next, we transformed the results to the time domain and used delay spread as a metric to quantify GO error. We also show that the pseudolateral wave manifests itself in the time domain as an additional pulse that arrives at a delay associated with the speed of a wave traveling in the lossy media. *INDEX TERMS:* 0624 Electromagnetics: Guided waves; 0689 Electromagnetics: Wave propagation (4275); 0609 Electromagnetics: Antennas; 0619 Electromagnetics: Electromagnetic theory; 0644 Electromagnetics: Numerical methods; *KEYWORDS:* geometric optics, indoor propagation channel, propagation over dielectric half plane, Sommerfeld integral, numerical electrodynamics, ray trace model

1. Introduction

[2] Ray tracing, based on the high-frequency geometric optics (GO) assumption, is a common method for approximating the transfer function of high-multipath radio channels. For indoor applications, however, antennas are likely to be mounted close to a wall or ceiling. Therefore the accuracy of conventional far-field concepts (e.g., antenna patterns, Fresnel reflection coefficients, and GO) are in question since antennas are only a few centimeters from dielectric surfaces. The intent of this article is to quantify the accuracy of GO for geometries relevant to the indoor environment; a more extensive presentation of this investigation is given by *Cotton et al.* [2000].

[3] We focus on the classic problem, dipole radiation above a lossy half-space, and consider the infinitesimal vertical electric dipole (VED) and *x*-aligned infinitesimal horizontal electric dipole (HED) as sources. Granted, infinitesimal dipoles are an oversimplification of any realistic antenna, but our intent is to analyze the limitations of geometric optics, not to assess near-field complications for specific antennas.

0048-6604/02/2000RS002508

Infinitesimal dipoles were chosen because general mathematical solutions as well as far-field approximations are well established. These equations provide a means of isolating GO error by observing the fundamental behavior of fields radiated for typical indoor geometries. In this study, we propose that GO is inadequate for modeling those scenarios that produce significant single-reflection error under practical frequency and geometric constraints.

[4] This article is organized in the following manner: First, the context is established with a brief summary of indoor channel characterization. In section 3, Sommerfeld's classical integral formulation along with conventional asymptotic expressions is given. Numerical techniques to evaluate Sommerfeld integrals are given in section 4, and frequency domain field strength results are given in section 5. The frequency domain results are transformed to a complex-baseband representation of the channel transfer function in order to calculate the channel impulse response. A detailed explanation of the time domain analyses is given in section 6, and corresponding results are shown in section 7.

2. Channel Characterization

[5] The number of indoor wireless local area network (WLAN) installations is growing; consequently, characterization of the indoor propagation channel has increased importance. This radio environment can be characterized in either the frequency or time domain. For a specific frequency band the channel transfer function is modeled via field strength predictions. In contrast, time domain modeling is based on the impulse response of the channel.

[6] For digital communications the impulse response is a quantity used to characterize the multipath propagation environment. Propagation effects on a transmitted signal are best described by a linear system re-presentation

$$b(t) = \int_{-\infty}^{+\infty} a(t-\tau)g(t,\tau)d\tau, \tag{1}$$

where $a(t)$ and $b(t)$ are the symbol waveforms before and after propagation through the channel, $g(t, \tau)$ is the time-variable impulse response of the propagation channel, and τ is the delay variable.

[7] Impulse response data are useful for the analysis and simulation of digital transmission because they quantify communication link degradation within a channel. More specifically, the delay spread τ_{spr} of a channel impulse response is a measure of time dispersion due to multipath and is defined as

$$\tau_{spr} = \sqrt{\frac{\int_{-\infty}^{+\infty} (\tau-\bar{\tau})^2 |g(t,\tau)|^2 d\tau}{\int_{-\infty}^{+\infty} |g(t,\tau)|^2 d\tau}}, \tag{2}$$

where $\bar{\tau}$ is the first moment or mean delay given by

$$\bar{\tau} = \frac{\int_{-\infty}^{+\infty} \tau |g(t,\tau)|^2 d\tau}{\int_{-\infty}^{+\infty} |g(t,\tau)|^2 d\tau}. \tag{3}$$

When calculating delay spread, measured values of $|g(t, \tau)|^2$ below a certain threshold are set to zero to nullify noise contribution. Throughout this article a threshold of -30 dB relative to the peak of the impulse is used for all delay spread calculations.

[8] Delay spread relative to symbol duration quantifies intersymbol interference. As a rule of thumb, small τ_{spr} indicates little degradation, whereas if τ_{spr} is large, then severe symbol distortion occurs. Historically, statistical analyses were used to deal with the time-variant channel [*Bello and Nelin*, 1963; *Greenstein and Prabhu*, 1979; *Jakes*, 1979; *Siller*, 1984; *Chuang*, 1987; *Devasirvatham*, 1987; *Burr*, 1996; *Wittmann et al.*, 1997]. In this article we are not interested in the time-variant nature of the channel, denoted by the dependent variable t in $g(t, \tau)$, or statistical procedures to account for this nature. Hence we treat the channel as deterministic and describe it with a single impulse response.

[9] Various computational approaches are used to approximate impulse response delay spread for indoor applications; some examples include ray trace models [*Lawton and McGeehan*, 1992, 1994; *Schauback et al.*, 1992; *Seidel and Rappaport*, 1992, 1994; *Holt et al.*, 1992; *Honcharenko et al.*, 1992; *Rappaport and Hawbaker*, 1992; *Yang et al.*, 1993; *Bronson et al.*, 1993; *Valenzuela*, 1993; *Kürner et al.*, 1994; *Durgin et al.*, 1997; *Chen and Jeng*, 1997; *Torres et al.*, 1999], simplified-decay models [*Holloway et al.*, 1999], and full numerical techniques (e.g., finite difference time domain) [*Talbi and Delisle*, 1996; *Lauer et al.*, 1995; *Taflove*, 1995; *Kunz and Luebbers*, 1993]. The most popular of these techniques is ray tracing, in which it is assumed that near-surface and near-field effects are negligible and that Fresnel reflection coefficients are valid.

3. Expressions for Radiation in Free Space Over Ground

[10] In order to isolate errors associated with the GO approximation for typical indoor scenarios, we focus on a single reflection off a planar surface. The classic

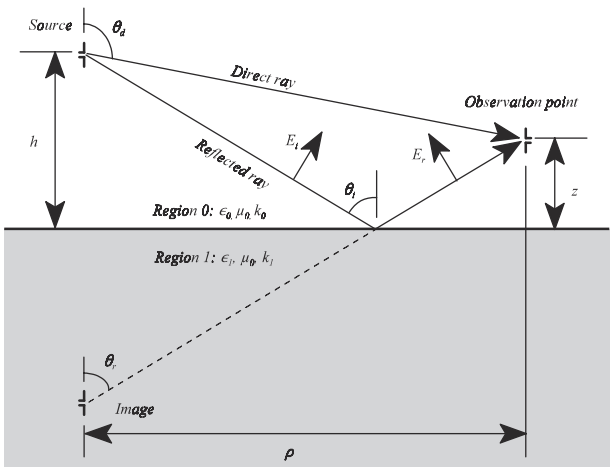

Figure 1. Parallel polarization geometry for electric fields above a dielectric half-space. Perpendicular-polarized electric fields are directed out of the page.

problem of infinitesimal dipole radiation above a ground plane has been analyzed extensively [*van der Pol*, 1935; *Norton*, 1937; *Sommerfeld*, 1964; *Baños*, 1966; *Tyras*, 1969; *Maclean and Wu*, 1993; *Wait*, 1998]. The geometry and nomenclature are shown in Figure 1. Region 0 is free space; the source dipole and receiver, regardless of nature and orientation, are located in region 0 at heights h and z above the boundary, respectively. Region 1 lies beneath the surface; its material composition is defined by its relative dielectric constant ϵ_r and conductivity σ. All media are assumed to be isotropic, homogeneous, and nonmagnetic.

[11] The general formulation of the two-media boundary problem is based on the solution of Maxwell's equations subject to boundary conditions at the interface. The differential form of Maxwell's equations, assuming $\exp(+j\omega t)$ harmonic time dependence for the fields, is

$$\nabla \times \mathbf{E} = -j\omega\mu_0\mathbf{H}, \qquad \nabla \times \mathbf{H} = \mathbf{J} + j\omega\epsilon\mathbf{E}\,, \quad (4)$$

where $\mathbf{E}$ is an electric field, $\mathbf{H}$ is a magnetic field, $\mathbf{J}$ is an impressed current source, capital letters denote time-harmonic fields (in contrast to time-instantaneous field variables, which are in lowercase), and boldface denotes a vector. The electric-type Hertz vector $\mathbf{\Pi}$ is useful for solving electromagnetic fields generated by a time-harmonic electric current; fields are expressed in terms of $\mathbf{\Pi}$ as

$$\mathbf{E} = k^2\mathbf{\Pi} + \nabla(\nabla \cdot \mathbf{\Pi}), \qquad \mathbf{H} = j\omega\epsilon\nabla \times \mathbf{\Pi}. \quad (5)$$

The corresponding Helmholtz wave equation is given by

$$\left(\nabla^2 + k^2\right)\mathbf{\Pi} = -\frac{\mathbf{J}}{j\omega\,\epsilon}, \quad (6)$$

where $k_1^2 = \omega^2\mu_0(\epsilon_r\epsilon_0 - j\sigma/\omega)$ defines the wave number of medium 1. Boundary conditions enforce continuity of tangential $\mathbf{E}$ and $\mathbf{H}$ components at the interface and allow for a unique solution of $\mathbf{\Pi}$.

3.1. Sommerfeld Formulation

[12] The classic Sommerfeld formulation for a dipole above a half plane is a general solution that contains complex, highly oscillatory integrals. The expressions were taken from *Baños* [1966] and are summarized in sections 3.1.1–3.1.2.

3.1.1. Vertical Electric Dipole

[13] An infinitesimal vertical current element placed a height h above the half plane produces a z-directed component of the vector potential in regions 0 and 1. For a VED, $\Pi_z(\rho, z)$ is independent of ϕ and only the E_z, E_ρ, and H_ϕ field components are radiated. Helmholtz equations in both media must be satisfied, and boundary conditions apply at the interface. Solution to the partial differential equation is simplified via double Fourier transform. Additionally, the specified geometry suggests a transformation to cylindrical coordinates that introduces a Bessel function into the integral solution. The resulting Sommerfeld formulation for the vector potential in region 0 is

$$\Pi_z = \frac{j\omega\mu_0 p}{4\pi k_0^2}\left[G_0 - G_1 + k_1^2 V\right], \quad (7)$$

where p is the dipole moment. The source and image Green's functions are defined as

$$G_0 = \frac{\exp(-jk_0R_0)}{R_0} = \int_0^\infty \frac{\exp[-l|h-z|]}{l} J_0(\xi\rho)\xi\, d\xi\,,$$
$$G_1 = \frac{\exp(-jk_0R_1)}{R_1} = \int_0^\infty \frac{\exp[-l(h+z)]}{l} J_0(\xi\rho)\xi\, d\xi, \quad (8)$$

respectively, where $J_0(\xi\rho)$ is the Bessel function of the first kind and order zero. The distances from the observation point to the source and image are

$$R_0 = \sqrt{\rho^2 + (z-h)^2}, \qquad R_1 = \sqrt{\rho^2 + (z+h)^2}, \quad (9)$$

respectively. The Sommerfeld integral V is defined as

$$V = \int_0^\infty \frac{2\exp[-l(z+h)]}{lk_1^2 + mk_0^2} J_0(\xi\rho)\xi\, d\xi, \quad (10)$$

and the functions l and m are given by

$$l = \sqrt{\xi^2 - k_0^2}, \qquad m = \sqrt{\xi^2 - k_1^2}. \quad (11)$$

Equation (7) is concise but not optimal for numerical evaluation given the electric properties of the reflecting surfaces considered in this article. An alternative form

was used by *van der Pol* [1935] and is given by

$$\Pi_z = \frac{j\omega\mu_0 p}{4\pi k_0^2}[G_0 + G_1 - 2Q], \tag{12}$$

where

$$Q = \int_0^\infty \frac{mk_0^2 \exp[-l(z+h)]}{l\left(lk_1^2 + mk_0^2\right)} J_0(\xi\rho)\xi\, d\xi\,. \tag{13}$$

Under this convention the sum $G_0 + G_1$ represents the situation when the ground is perfectly conducting and the Sommerfeld integral Q represents a correction for the lossy characteristics of ground. For the material properties considered, equation (12) significantly reduces the magnitude of the integrand in equation (13) and consequently improves the convergence and accuracy of the numerical integration.

[14] Relevant field components are extracted from equation (5) to form the following field expressions:

$$\begin{aligned} E_z &= \frac{j\omega\mu_0 p}{4\pi k_0^2}\left[\left(\frac{\partial^2}{\partial z^2} + k_0^2\right)(G_0 + G_1 - 2Q)\right], \\ E_\rho &= \frac{j\omega\mu_0 p}{4\pi k_0^2}\left[\frac{\partial^2}{\partial\rho\,\partial z}(G_0 + G_1 - 2Q)\right], \\ H_\phi &= \frac{p}{4\pi}\left[\frac{\partial}{\partial\rho}(G_0 + G_1 - 2Q)\right]. \end{aligned} \tag{14}$$

These general expressions were derived with no assumptions regarding proximity, wavelength, or material composition; they account for the near-surface and near-field effects we aim to observe.

3.1.2. Horizontal Electric Dipole

[15] In the case of an infinitesimal horizontal current element placed a height h above the half plane in the x direction, *Baños* [1966] employs the x and z components of the electric Hertz vector (i.e., $\mathbf{\Pi} = \mathbf{a}_x\Pi_x + \mathbf{a}_z\Pi_z$). The z components satisfy the homogeneous Helmholtz equation in each medium, and the x components satisfy the inhomogeneous Helmholtz equation in region 0 and the homogeneous Helmholtz equation in region 1. Application of the boundary conditions at the interface gives vector potential solutions for region 0 that are substituted into equation (5) to give field expressions. Sommerfeld formulations of the transverse electric (TE) field components are

$$\begin{aligned} E_\phi &= \frac{j\omega\mu_0 p}{4\pi k_0^2}\sin\phi\left[\frac{1}{\rho}\frac{\partial}{\partial\rho}\left(G_0 - G_1 + k_0^2 V\right)\right. \\ &\quad \left. + k_0^2(G_0 - G_1 + U)\right], \\ H_z &= -\frac{p}{4\pi}\sin\phi\left[\frac{\partial}{\partial\rho}(G_0 - G_1 + U)\right], \\ H_\rho &= \frac{p}{4\pi}\sin\phi\left[\frac{\partial}{\partial z}(G_0 - G_1 + U) - \frac{1}{\rho}\frac{\partial W}{\partial\rho}\right], \end{aligned} \tag{15}$$

and the transverse magnetic (TM) field components are

$$\begin{aligned} E_z &= -\frac{j\omega\mu_0 p}{4\pi k_0^2}\cos\phi\left[\frac{\partial^2}{\partial z\partial\rho}\left(G_0 + G_1 - k_1^2 V\right)\right], \\ E_\rho &= -\frac{j\omega\mu_0 p}{4\pi k_0^2}\cos\phi\left[\frac{\partial^2}{\partial\rho^2}\left(G_0 - G_1 + k_0^2 V\right)\right. \\ &\quad \left. + k_0^2(G_0 - G_1 + U)\right], \\ H_\phi &= \frac{p}{4\pi}\cos\phi\left[\frac{\partial}{\partial z}(G_0 - G_1 + U) - \frac{\partial^2 W}{\partial\rho^2}\right], \end{aligned} \tag{16}$$

Sommerfeld integrals U and W are defined by

$$\begin{aligned} U &= \int_0^\infty \frac{2\exp[-l(z+h)]}{l+m} J_0(\xi\rho)\xi\, d\xi\,, \\ W &= \int_0^\infty \frac{2(l-m)\exp[-l(z+h)]}{k_1^2 l + k_0^2 m} J_0(\xi\rho)\xi\, d\xi\,. \end{aligned} \tag{17}$$

Note that if one were to compare the VED and HED Sommerfeld formulations given in this article to the corresponding expressions given by *Baños* [1966], then a number of differences would be observed. These differences are due to an opposite time convention and rotation of the spatial coordinate axes. The opposite time convention causes the opposite sign in the exponent of G_0 and G_1. Rotation of the coordinate axes flips the leading sign of many of the field equations, the sign in front of z in numerous exponential exponents, and the sign of W.

3.2. Geometric Optics and Norton Surface Wave Approximation

[16] Special cases exist where closed-form approximations are obtainable. Geometric optics is a far-field approximation, and Norton surface wave terms may be used to approximate surface wave effects.

3.2.1. Vertical Electric Dipole

[17] If the observation point is in the far field of the source, then the approximations to fields resulting from a vertical electric dipole above a half plane are given by

$$\begin{aligned} E_z \approx -\frac{jk_0 p}{4\pi}\sqrt{\frac{\mu_0}{\epsilon_0}}\left[\sin^2\theta_d G_0 + \Gamma_\parallel \sin^2\theta_r G_1\right. \\ \left. + \left(1 - \Gamma_\parallel\right) F(w)\sin^2\theta_r G_1\right], \end{aligned}$$

$$E_\rho \approx \frac{jk_0p}{4\pi}\sqrt{\frac{\mu_0}{\epsilon_0}}\left[\sin\theta_d\cos\theta_d G_0 + \Gamma_\parallel \sin\theta_r\cos\theta_r G_1 - \left(1-\Gamma_\parallel\right)\Delta_0 F(w)\sin\theta_r G_1\right],$$

$$H_\phi \approx \frac{jk_0p}{4\pi}\left[\sin\theta_d G_0 + \Gamma_\parallel \sin\theta_r G_1 + \left(1-\Gamma_\parallel\right)F(w)\sin\theta_r G_1\right], \tag{18}$$

where θ_d and θ_r are shown in Figure 1. The first two terms make up the GO approximation, which involves the Fresnel reflection coefficient $\Gamma_\parallel$. The third term is Norton's surface wave approximation, which was obtained from a high-refractivity, far-field approximation to V [*Norton*, 1937]. The Norton term incorporates an attenuation function given by

$$F(w) = 1 - \sqrt{\pi w}\, e^{-w}\,\mathrm{erfc}\left(j\sqrt{w}\right). \tag{19}$$

For a homogeneous half-space the remaining variables are defined as

$$w = -\frac{jk_0R_0}{2\sin^2\theta_r}\left(\cos\theta_r + \Delta_0\right)^2,$$
$$\Delta_0 = \frac{k_0}{k_1}\sqrt{1-\left(\frac{k_0}{k_1}\right)^2\sin^2\theta_r}. \tag{20}$$

Norton surface wave terms are valid only when $k_0R_0 \gg 1$ and $|k_1| > |k_0|$ because of assumptions made when deriving equations (18), (19), and (20).

3.2.2. Horizontal Electric Dipole

[18] For observation points in the far field of a horizontal dipole above a homogeneous half plane, the TE fields are given by

$$E_\phi \approx \frac{jk_0p}{4\pi}\sqrt{\frac{\mu_0}{\epsilon_0}}\sin\phi[G_0 + \Gamma_\perp G_1 + (1-\Gamma_\perp)F(q)G_1],$$

$$H_z \approx \frac{jk_0p}{4\pi}\sin\phi[\sin\theta_d G_0 + \Gamma_\perp\sin\theta_r G_1 + (1-\Gamma_\perp)F(q)\sin\theta_r G_1], \tag{21}$$

$$H_\rho \approx -\frac{jk_0p}{4\pi}\sin\phi[\cos\theta_d G_0 + \Gamma_\perp\cos\theta_r G_1 - (1-\Gamma_\perp)F(q)\delta_0 G_1],$$

and the TM components in the far field are given by

$$E_z \approx \frac{jk_0p}{4\pi}\sqrt{\frac{\mu_0}{\epsilon_0}}\cos\phi\left[\sin\theta_d\cos\theta_d G_0 - \Gamma_\parallel\sin\theta_r\cos\theta_r G_1 + \left(1-\Gamma_\parallel\right)F(w)\Delta_0\sin\theta_r G_1\right],$$

$$E_\rho \approx -\frac{jk_0p}{4\pi}\sqrt{\frac{\mu_0}{\epsilon_0}}\cos\phi\left[\cos^2\theta_d G_0 - \Gamma_\parallel\cos^2\theta_r G_1 - \left(1-\Gamma_\parallel\right)F(w)\Delta_0^2 G_1\right],$$

$$H_\phi \approx -\frac{jk_0p}{4\pi}\cos\phi\left[\cos\theta_d G_0 - \Gamma_\parallel\cos\theta_r G_1 + \left(1-\Gamma_\parallel\right)F(w)\Delta_0 G_1\right], \tag{22}$$

where θ_d and θ_r are shown in Figure 1, the sum of the first two terms is the geometric optics approximation, and the third term is the Norton surface wave term. For a homogeneous half-space the remaining variables are defined as

$$q = -\frac{jk_0R_0}{2\sin^2\theta_r}\left(\cos\theta_r + \delta_0\right)^2,$$
$$\delta_0 = \frac{k_1}{k_0}\sqrt{1-\left(\frac{k_0}{k_1}\right)^2\sin^2\theta_r}. \tag{23}$$

Similar to the VED case, the Norton surface wave terms are valid only when $k_0R_0 \gg 1$ and $|k_1| > |k_0|$. Section 3.2.3 provides a summary of Fresnel reflection coefficients to complete the far-field formulation of the fields radiated by infinitesimal dipoles above a half-space.

3.2.3. Fresnel Reflection Coefficients

[19] Detailed derivations for the expressions given in this section may be found in standard electromagnetic texts, such as that by *Johnk* [1988]. Electric field polarization is defined relative to the plane of incidence, which contains the normal to the reflecting surface and the incident propagation vector. Parallel polarized electric fields lie in the plane of incidence, and perpendicular polarized fields are orthogonal. The E field Fresnel reflection coefficients at a plane boundary are

$$\Gamma_\parallel = \frac{\eta_0\cos\theta_i - \eta_1\cos\theta_t}{\eta_0\cos\theta_i + \eta_1\cos\theta_t}, \quad \Gamma_\perp = \frac{\eta_1\cos\theta_i - \eta_0\cos\theta_t}{\eta_1\cos\theta_i + \eta_0\cos\theta_t}, \tag{24}$$

where the transmitted angle and intrinsic wave impedance of region 1 are complex and defined as

$$\sin\theta_t = \frac{\eta_1}{\eta_0}\sin\theta_i, \qquad \eta_1 = \sqrt{\frac{\mu_0}{\epsilon_r\epsilon_0 - j\sigma/\omega}}, \tag{25}$$

respectively.

4. Numerical Integration Techniques

[20] To evaluate the accuracy of GO, we analyze near-field interaction and propagation effects near the interface. General solutions for fields radiated by a VED or an

x-aligned HED are obtained via numerical evaluation of Sommerfeld integrals. In this section, relevant numerical techniques are discussed; further details are given by *Lytle and Lager* [1974], *Johnson and Dudley* [1983], *Press et al.* [1986], *Mosig* [1989], and *Michalski* [1998].

4.1. Romberg Quadrature

[21] Romberg integration is an effective means of integrating well-behaved integrands over a finite range of integration. It uses Neville's algorithm to extrapolate the error from previous predictions and subtracts off that error to give a higher-order approximation [*Press et al.*, 1986].

4.2. Weighted-Averages Method

[22] The weighted-averages method is a useful numerical technique for integrating functions that are periodic yet convergent over a semi-infinite integration range. Sommerfeld integrals are inherently oscillatory and slowly convergent because of the presence of Bessel functions. We begin our discussion of the weighted-averages method with the integration then summation technique [*Michalski*, 1998], where the integral is expressed as a limit of a sequence of partial sums

$$S = \int_{\xi_{-1}}^{\infty} \mathrm{X}(\xi)\, d\xi = \int_{\xi_{-1}}^{\infty} \chi(\xi) J_{\upsilon}(\xi\rho)\xi\, d\xi$$

$$= \lim_{N\to\infty} \sum_{n=0}^{N} \int_{\xi_{n-1}}^{\xi_n} \chi(\xi) J_{\upsilon}(\xi\rho)\xi\, d\xi = \lim_{N\to\infty} S_N. \qquad (26)$$

Note that the Sommerfeld integrand X was split into its characteristic factors (i.e., χ, J_ν, and ξ). The lower integration limit, ξ_{-1}, is chosen to ensure that no singularities exist in the Sommerfeld tail $X(|\mathcal{R}\xi| > |\xi_{-1}|)$. The sequence S_N approaches S slowly, and the error or remainder complies with the following expression:

$$r_N = S_N - S = -\int_{\xi_N}^{\infty} \chi(\xi) J_{\upsilon}(\xi\rho)\xi\, d\xi$$

$$\sim w_N \sum_{n=0}^{\infty} c_n \xi_N^{-n} \qquad N \to \infty, \qquad (27)$$

where w_N are remainder estimates specific to $\chi(\xi)$. Series acceleration methods are based on the idea that information contained in the sequence of partial sums, $S_0, S_1, \ldots, S_N$, is extracted and utilized in a way that is more efficient than conventional combination techniques. If the weight, W_N, is associated with S_N, then a general combination formula is

$$S'_N = \frac{W_N S_N + W_{N+1} S_{N+1}}{W_N + W_{N+1}} = S + \frac{W_N r_N + W_{N+1} r_{N+1}}{W_N + W_{N+1}}$$

$$= S + r'_N. \qquad (28)$$

The second expression shows that if

$$\alpha_N \equiv \frac{W_{N+1}}{W_N} = -\frac{r_N}{r_{N+1}}, \qquad (29)$$

then the remainder r'_N of the transformed sequence will be nullified. The difficulty is determining r_N from its asymptotic estimates. Careful scrutiny leads to the generalized weighted-averages algorithm, given as

$$S_N^{(\ell+1)} = \frac{S_N^{(\ell)} + \alpha_N^{(\ell)} S_{N+1}^{(\ell)}}{1 + \alpha_N^{(\ell)}} \qquad N \geq 0 \text{ and } \ell \geq 0, \quad (30)$$

where parenthesized superscripts denote transformation order and $\alpha_N^{(\ell)}$ is formulated in section 4.3 for the integrands under consideration. Equation (30) is a recursive scheme that produces $S_0^{(\ell)}$ as the best approximation to S, given the partial sums $S_0, S_1, \ldots, S_\ell$, and accelerates the convergence.

4.3. Numerical Evaluation of $2Q/k_0^2$, U, V, and W

[23] Efficient numerical integration of the integrals associated with dipole radiation above a half plane are now considered. Table 1 summarizes the necessary Sommerfeld integrals, and Figure 2 illustrates the common traits among each of the integrands in the complex plane. Derivatives were pulled inside the integrals, and each resulting Sommerfeld integrand X contains Bessel functions, exponential terms, branch cuts, and possible poles. These factors make analytic solutions unlikely but provide a commonality which allows for a single numerical integration scheme to evaluate all of the integrals. In this approach the real-axis integration path is partitioned, and specific numerical integration techniques are used according to the integrand behavior in each subinterval.

[24] Poles may cause strong variations in the integrand, such as those associated with V and W at

$$\xi_{\mathrm{pole}} = \frac{\pm k_0 k_1}{\sqrt{k_0^2 + k_1^2}}. \qquad (31)$$

These poles are located in the fourth quadrant on the complex plane just below the real axis and $\Re(\xi_{\mathrm{pole}}) \leq k_0$ as well as in the second quadrant symmetric about the origin. It was confirmed that they have negligible effect on the real-axis integration path for the electric properties considered.

[25] To avoid branch cuts, the integration path was partitioned into the three subintervals $[0, k_0]$, $[k_0, k_0\sqrt{\epsilon_r}]$ and $[k_0\sqrt{\epsilon_r}, \infty]$. Different techniques were used accord-

Table 1. Sommerfeld Integrands and Asymptotic Coefficients

Sommerfeld	Sommerfeld Integrand X	Asymptotic
$\frac{2Q}{k_0^2}$	$\frac{2\,m\exp[-l(z+h)]}{l\left(k_0^2\,m+k_1^2\,l\right)}J_0(\xi\rho)\xi$	1
$\frac{\partial^2}{\partial z^2}\left(\frac{2Q}{k_0^2}\right)$	$\frac{2l\,m\exp[-l(z+h)]}{k_0^2\,m+k_1^2\,l}J_0(\xi\rho)\xi$	-1
$\frac{\partial^2}{\partial z\,\partial\rho}\left(\frac{2Q}{k_0^2}\right)$	$\frac{2\,m\exp[-l(z+h)]}{k_0^2\,m+k_1^2\,l}J_1(\xi\rho)\xi^2$	-1
$\frac{\partial}{\partial\rho}\left(\frac{2Q}{k_0^2}\right)$	$-\frac{2\,m\exp[-l(z+h)]}{l\left(k_0^2\,m+k_1^2\,l\right)}J_1(\xi\rho)\xi^2$	0
$\frac{\partial^2 V}{\partial z\,\partial\rho}$	$\frac{2l\exp[-l(z+h)]}{k_0^2m+k_1^2l}J_1(\xi\rho)\xi^2$	-1
$\frac{\partial V}{\partial\rho}$	$-\frac{2\exp[-l(z+h)]}{k_0^2m+k_1^2l}J_1(\xi\rho)\xi^2$	0
$\frac{\partial^2 V}{\partial\rho^2}$	$\frac{2\exp[-l(z+h)]}{k_0^2m+k_1^2l}\left[\frac{J_1(\xi\rho)}{\rho}-\xi J_0(\xi\rho)\right]\xi^2$	0, -1
U	$\frac{2\exp[-l(z+h)]}{l+m}J_0(\xi\rho)\xi$	1
$\frac{\partial U}{\partial z}$	$-\frac{2l\exp[-l(z+h)]}{l+m}J_0(\xi\rho)\xi$	0
$\frac{\partial U}{\partial\rho}$	$-\frac{2\exp[-l(z+h)]}{l+m}J_1(\xi\rho)\xi^2$	0
$\frac{\partial W}{\partial\rho}$	$-\frac{2(l-m)\exp[-l(z+h)]}{k_0^2m+k_1^2l}J_1(\xi\rho)\xi^2$	-1
$\frac{\partial^2 W}{\partial\rho^2}$	$\frac{2(l-m)\exp[-l(z+h)]}{k_0^2m+k_1^2l}\left[\frac{J_1(\xi\rho)}{\rho}-\xi J_0(\xi\rho)\right]\xi^2$	-1, -2

ing to specific difficulties encountered in each subinterval. In the first subinterval, change of variables $\xi = k_0\cos u$ removed the discontinuity in the derivative at k_0, resulting in

$$\int_0^{k_0} \mathrm{X}(\xi)\,d\xi = \int_0^{\pi/2} \mathrm{X}(k_0\cos u)k_0\sin u\,du. \tag{32}$$

Change in variable $\xi = k_0\cosh v$ removed the discontinuity at k_0 in the second subinterval, giving

$$\int_{k_0}^{k_0\sqrt{\epsilon_r}} \mathrm{X}(\xi)d\xi = \int_0^{\mathrm{Arccosh}\sqrt{\epsilon_r}} \mathrm{X}(k_0\cosh v)k_0\sinh v\,dv. \tag{33}$$

The integrands in equations (32) and (33) are well behaved and converge when numerically integrated with Romberg quadrature.

[26] The semi-infinite subinterval was chosen to begin at $\xi_{-1} = k_0\sqrt{\epsilon_r}$ because all singularities, poles, and branch points on the right half of the complex plane lie either on or to the left of the line defined by $\Re(\xi) = k_0\sqrt{\epsilon_r}$. Change in variable was not necessary, and the generalized weighted-averages algorithm was used to numerically integrate the Sommerfeld integral tail. Breakpoints were chosen at $\xi_N = k_0\sqrt{\epsilon_r} + N\pi/\rho$, based on the half-period of the Bessel function π/ρ, and weights were chosen according to the analytical form of the remainder estimates, given by

$$w_N = \frac{(-1)^{N+1}}{\xi_N^{\beta-1/2}}\exp\left[-\frac{N\pi(z+h)}{\rho}\right]. \tag{34}$$

[27] A detailed derivation of equation (34) was given by *Michalski* [1998]. This equation is based on the asymptotic behavior of the Sommerfeld integrand, which

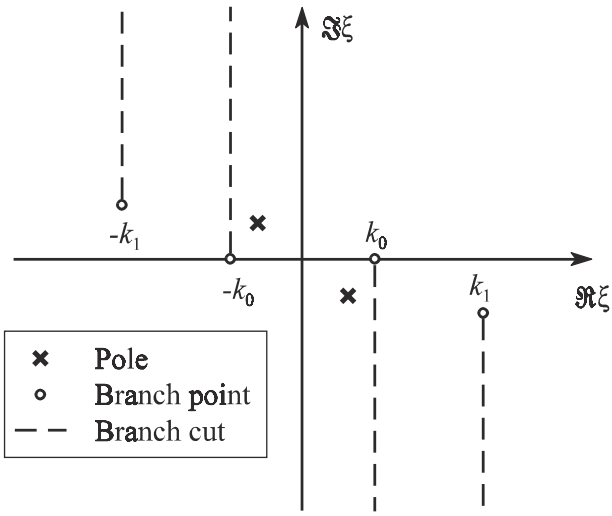

Figure 2. Sommerfeld poles and branch points in complex plane.

is characterized by the asymptotic coefficient β (given in Table 1) and the expressions

$$f(\xi) \sim \frac{\exp[-\xi(z+h)]}{\xi^{\beta}}\left[C + O\left(\xi^{-1}\right)\right],$$
$$J_{\upsilon}(\xi\rho) \sim \sqrt{\frac{2}{\pi\xi\rho}}\cos\left(\xi\rho - \upsilon\frac{\pi}{2} - \frac{\pi}{4}\right), \tag{35}$$

where C is a constant. Applying equation (34) to equations (27) and (29) gives

$$\alpha_N^{(\ell)} = \exp\left[\frac{\pi(z+h)}{\rho}\right]\left(\frac{\xi_{N+1}}{\xi_N}\right)^{\beta-1/2+\ell}, \tag{36}$$

which completes the weighted-averages formulation given by equation (30).

5. Frequency Domain Results

[28] In this section, field strength results and corresponding GO errors are illustrated in the frequency domain. Frequencies ranging from 10 to 8000 MHz (i.e., $30 \geq \lambda \geq 0.0375$ m) were chosen to encompass the industrial, scientific, and medical (ISM) bands at 902–928 MHz, 2.4000–2.4835 GHz, and 5.725–5.850 GHz where unlicensed wireless local area network products operate [*LaMaire et al.*, 1996].

[29] In order for the theoretical received signals to embody the channel transfer function, we simulate a flat-frequency transmitted spectrum by defining the electric dipole moment as

$$p = j\frac{4\pi}{\omega\mu_0}. \tag{37}$$

Depending on the type and orientation of the receive antenna, one or some combination of the field components will be the dominant coupling mechanism. Orientation, radiation pattern, and efficiencies of the receive antenna are fairly arbitrary and only clutter the field effects we wish to observe. We examine each field component at the observation point separately in order to generalize the results and allow for various receive antenna polarizations to be easily realized.

[30] Throughout this article, superscripts (i.e., E_z^S, E_z^{GO}, $E_z^{\mathrm{GO}+N}$) and colors (i.e., green, red, blue) are used to distinguish between Sommerfeld, GO, and GO with Norton term results. Note that in many plots the curves are indistinguishable because they lie on top of one another.

5.1. Conductivity Variation to Demonstrate Two-Ray Behavior

[31] Electric properties are defined by the conductivity and relative dielectric constant of the lossy half-space; geometry is specified by height above the interface and horizontal separation. In this section, we consider $\{\sigma\} = \{0.00195, 0.195, 19.5, 1950\}$ S/m, $\epsilon_r = 5$, and $\{h, z, \rho\} = \{1, 1, 10\}$ m in order to minimize the effect of the null in the radiation pattern of the VED source and to ideally illustrate the nature of the two-ray model. Figure 3 presents the Sommerfeld solution and the GO approximation to E_z field strength radiated by a VED for this geometry.

[32] As the electrical conductivity gets large, the Fresnel reflection coefficients approach plus or minus unity and the field expressions approach the sum of the source and image Green's functions $G_0 + G_1$. This produces a two-ray cancellation effect, where equally spaced nulls occur according to the difference in path lengths, $\Delta R = R_1 - R_0$. At lower conductivities the reflected wave is less influential because the Fresnel reflection coefficient decreases in magnitude and shifts in phase, thus flattening the cancellation behavior and shifting the nulls in frequency.

[33] For practical purposes we limit the scope of the remainder of this analysis to reflecting surfaces made of concrete. Although the electric properties of concrete vary with frequency [*Halabe et al.*, 1993], we assume that frequency-independent parameters (i.e., $\epsilon_r = 5$ and $\sigma = 0.00195$ S/m) will provide representative results.

5.2. Position Variation to Isolate Near-Surface and Near-Field Effects

[34] In this section, we position the source and observation points to isolate near-surface and near-field

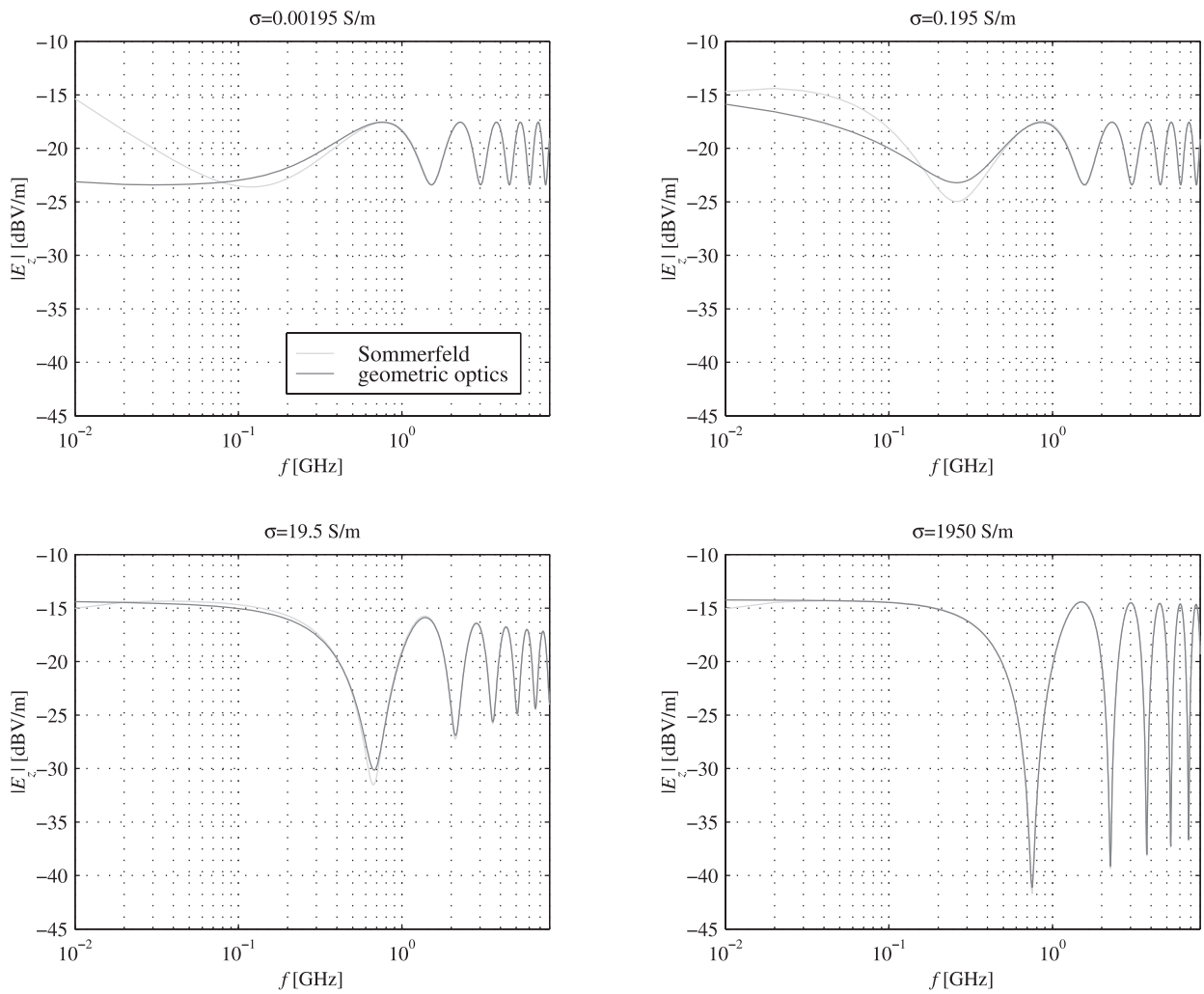

Figure 3. Electric field strength (z component) for a VED above a half-space ($z = h = 1$ m, $\rho = 10$ m, $\epsilon_r = 5$) at various conductivities. See color version of this figure at back of this issue.

effects. Figures 4 and 5 illustrate fields radiated by a VED above a half plane, Figures 6 and 7 isolate the TE waves of an x-aligned HED by limiting the observation points to $\phi = 90°$, and Figures 8 and 9 isolate the TM waves of an x-aligned HED by limiting the observation points to $\phi = 0°$.

[35] For infinitesimal electric dipoles, simulations show that near-field effects are substantially reduced for $\rho > 1$ m excluding the E_ρ component of the HED-TM case; hence we isolate near-surface effects by holding the horizontal separation constant at 5 m and simultaneously reducing the source and observation heights: $\{(h, z, \rho)\} = \{(10, 10, 5), (1, 1, 5), (0.1, 0.1, 5), (0.01, 0.01, 5)\}$ m. Figures 4, 6, and 8 demonstrate surface effects on field strength.

[36] It will be shown in section 7.1 that for an infinitesimal electric dipole above a concrete half plane, surface effects are significantly reduced when $h \geq 10$ m and $z \geq 10$ m. Therefore we isolate near-field effects by holding the source and observation points at a constant height of 10 m and reducing the horizontal separation: $\{(h, z, \rho)\} = \{(10, 10, 10), (10, 10, 1), (10, 10, 0.1), (10, 10, 0.01)\}$ m. Figures 5, 7, and 9 illustrate near-field effects in the frequency domain.

5.2.1. Surface Wave

[37] Norton surface wave terms provide a means to isolate surface wave effects (observe blue curves in Figures 4, 6, and 8). Near the interface, deviation from geometric optics due to surface wave propagation peaks

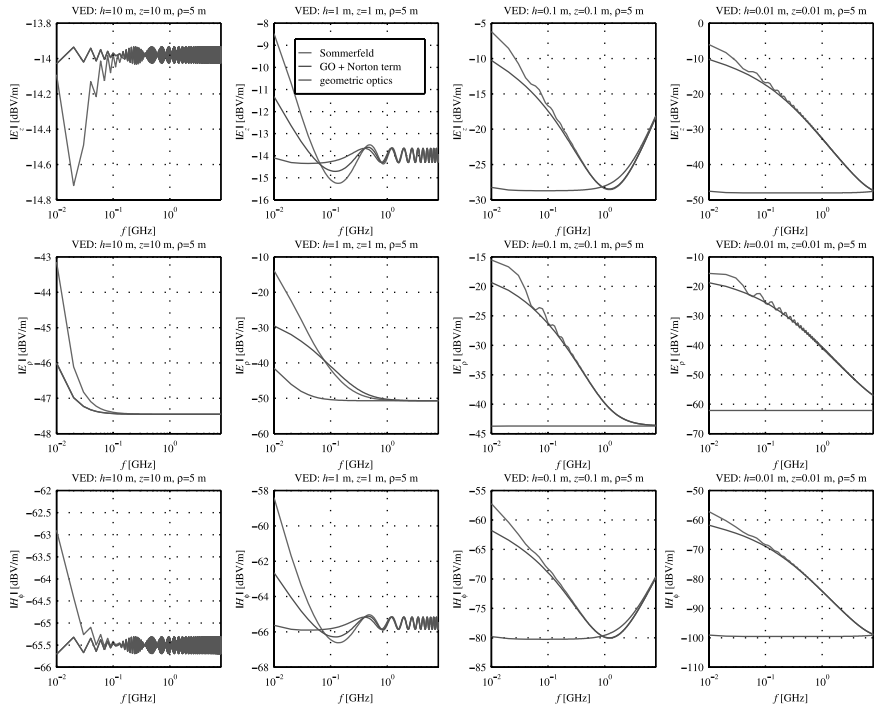

Figure 4. Near-surface effects on field strength of a VED above a concrete half-space. See color version of this figure at back of this issue.

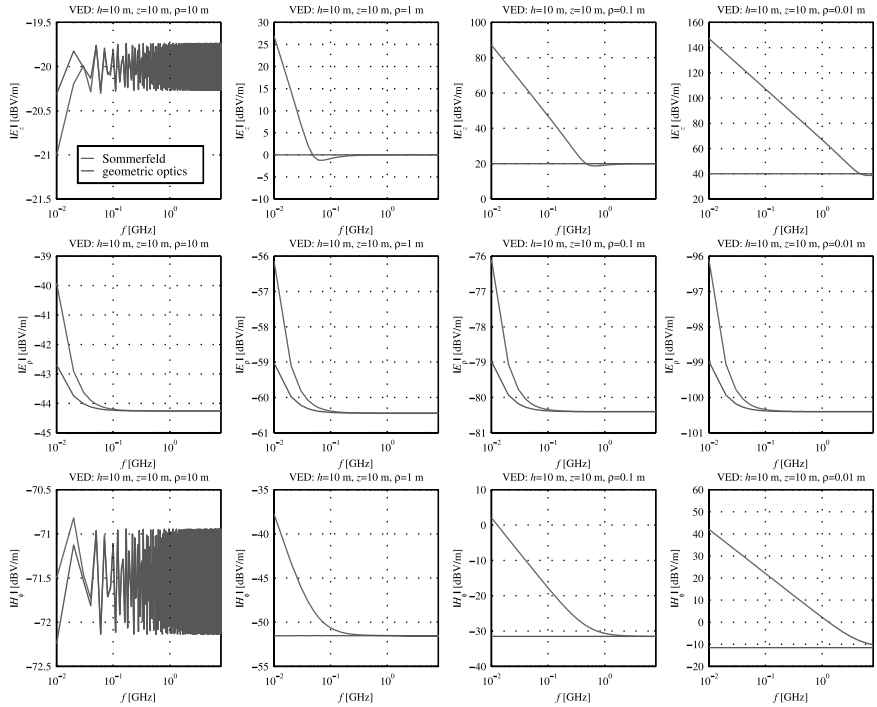

Figure 5. Near-field effects on field strength of a VED above a concrete half-space. See color version of this figure at back of this issue.

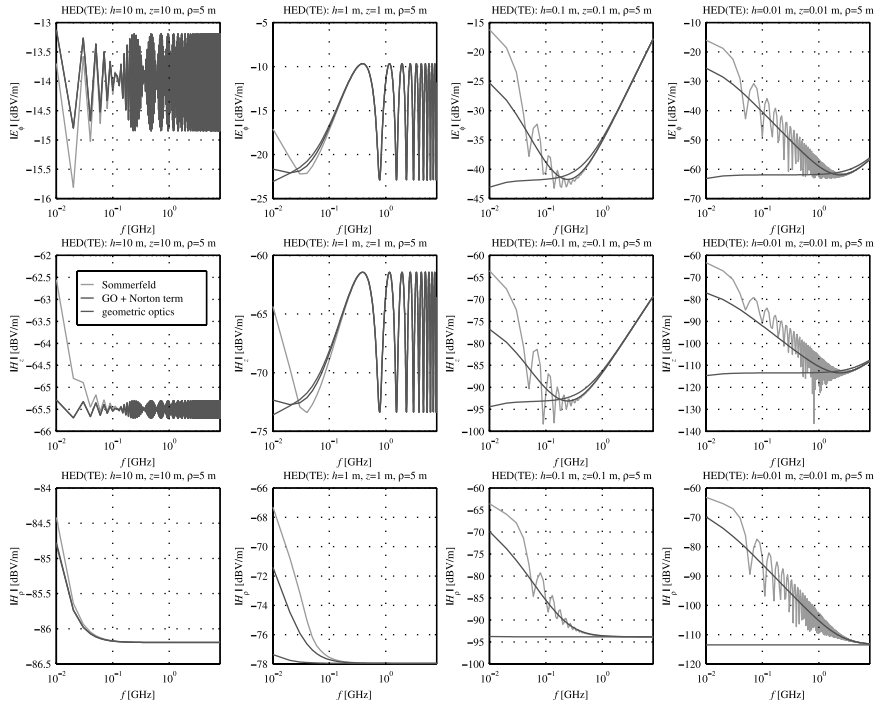

Figure 6. Near-surface effects on TE field strength of an *x*-aligned HED above a concrete half-space. Observation points are restricted to $\phi = 90°$. See color version of this figure at back of this issue.

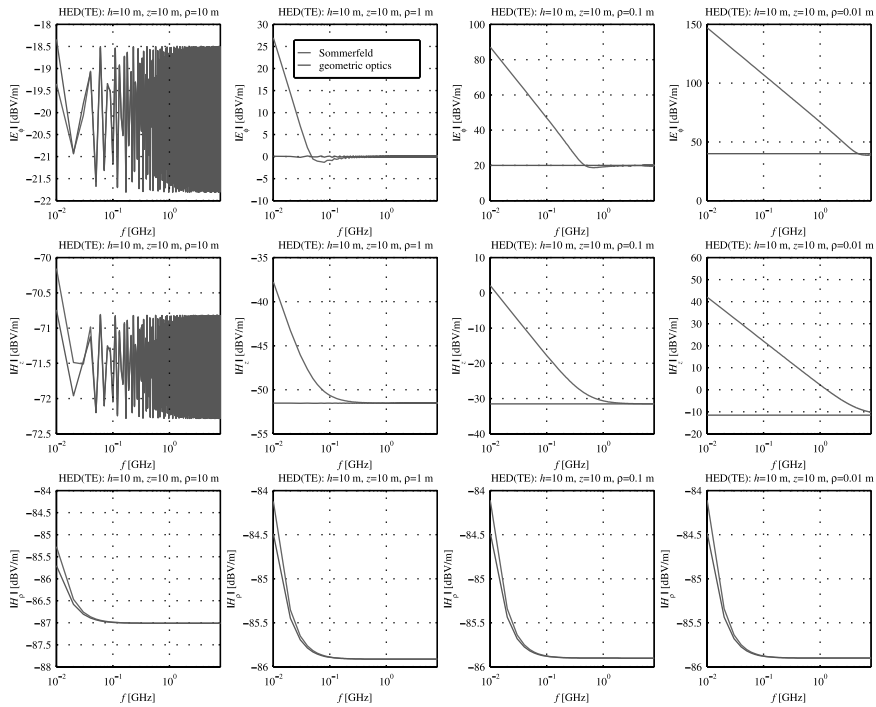

Figure 7. Near-field effects on TE field strength of an *x*-aligned HED above a concrete half-space. Observation points are restricted to $\phi = 90°$. See color version of this figure at back of this issue.

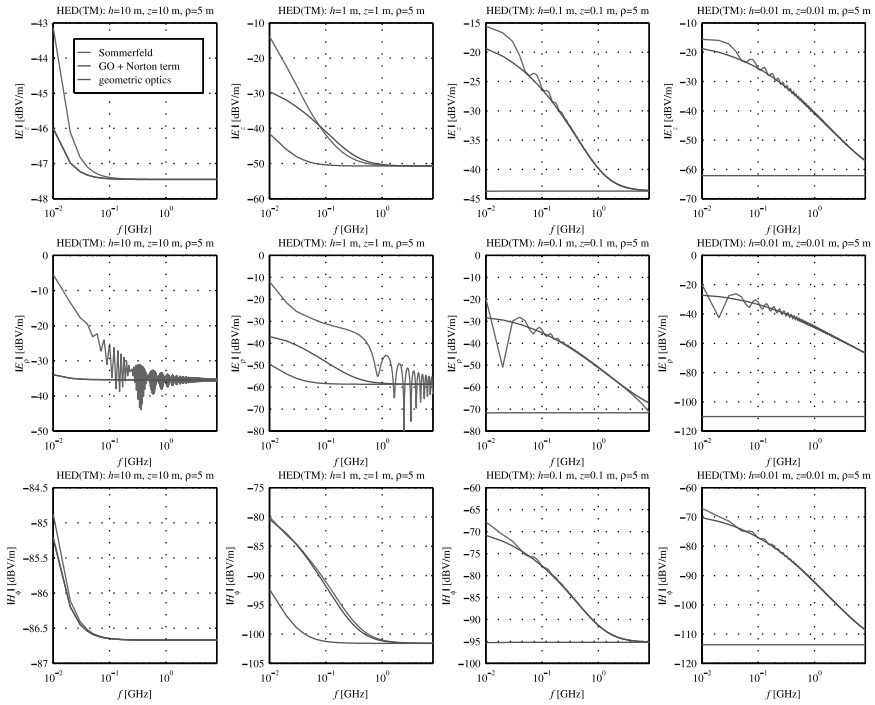

Figure 8. Near-surface effects on TM field strength of an *x*-aligned HED above a concrete half-space. Observation points are restricted to $\phi = 0°$. See color version of this figure at back of this issue.

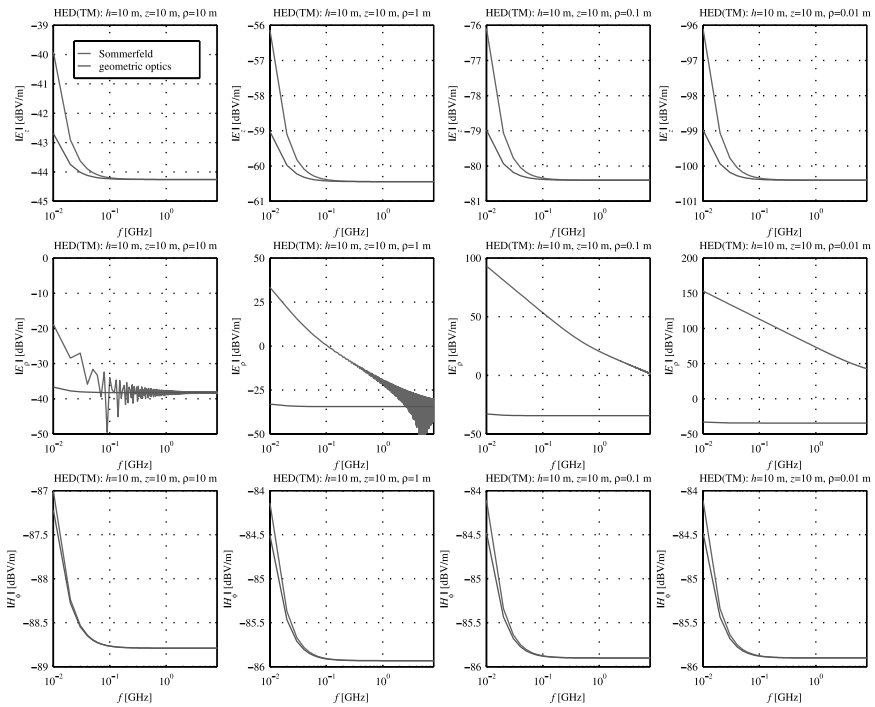

Figure 9. Near-field effects on TM field strength of an *x*-aligned HED above a concrete half-space. Observation points are restricted to $\phi = 0°$. See color version of this figure at back of this issue.

near zero hertz (i.e., DC) and decreases continuously with increasing frequency. As expected, surface wave propagation is more influential in fields radiated by VED and in TM fields radiated by HED. In comparison to the more general Sommerfeld solution, GO plus Norton term approximations seem adequate for predicting the radiation of a VED above a half plane; significant discrepancies, however, appear in the HED case where oscillations are observed and when near-field effects are influential.

5.2.2. Pseudolateral Wave

[38] Sommerfeld results in Figure 6 show strong oscillations in the TE fields radiated by an *x*-aligned HED over a wide range of frequencies when the source and observation point are near the interface (i.e., $h \leq 0.1$ m and $z \leq 0.1$ m). With reference to *Kuester and Chang* [1979], alternative expressions for U, V, and W are provided to help explain this oscillation.

[39] Notice that the HED-TE fields in equation (15) are strongly influenced by the integral U. Rationalization of the denominator in U and use of the integral representation of G_1 in equation (8) allows for it to be rewritten as

$$U = \frac{2}{k_1^2 - k_0^2}\left[\frac{\partial^2 G_1}{\partial z^2} - \int_0^\infty m \exp[-l(z+h)] J_0(\xi\rho)\xi\, d\xi\right]. \tag{38}$$

If we add and subtract 1 within the integrand and make use of

$$\int_0^\infty m J_0(\xi\rho)\xi\, d\xi = \frac{\partial^2}{\partial z^2}\frac{\exp[-jk_1R_1]}{R_1}\bigg|_{z=h=0}, \tag{39}$$

then U can be expressed as

$$U = \frac{2}{k_1^2 - k_0^2}\left[\frac{\partial^2 G_1}{\partial z^2} - \frac{\partial^2}{\partial z^2}\frac{\exp(-jk_1R_1)}{R_1}\bigg|_{z=h=0} - \int_0^\infty m\{\exp[-l(z+h)]-1\} J_0(\xi\rho)\xi\, d\xi\right] \tag{40}$$

Close to the interface the integral term is relatively small, and the first two terms depict two waves traveling adjacent to one another but at different speeds due to the different propagation media. The two waves destructively interfere when $-k_0R_1 \approx -k_1R_1 + 2\pi n$, where n is an integer. For the material properties chosen and $R_1 = 5$ m the interference occurs approximately every 48.5 MHz, which agrees with the oscillation observed. The interference caused by the adjacent fields dies off quickly as the source and observation point are moved away from the surface. This suggests near-field excitation for generating this phenomenon, which we call a pseudolateral wave for reasons made clear below.

[40] By the same motivation an alternative form of the Sommerfeld integral V is derived. Add and subtract 1 within the integrand in equation (10). The denominator of V cannot be rationalized as with U, but the integral identity

$$\int_{k_0/k_1}^{k_1/k_0} \frac{v\, dv}{\sqrt{\left(\xi^2 - \xi_{\text{pole}}^2\right)v^2 - \xi_{\text{pole}}^2}} = \frac{k_1^4 - k_0^4}{k_1k_0}\frac{1}{k_1^2 l + k_0^2 m} \tag{41}$$

allows for integration by parts, which produces two additive exponential terms. Finally, change in variable and identification of the integral form of the incomplete Hankel function, given by

$$H_0^{(1)}(k_1/k_0, \xi\rho) = \frac{2}{j\pi}\int_0^{k_1/k_0} \frac{\exp\left(j\xi\rho\sqrt{1+u^2}\right)}{\sqrt{1+u^2}} du, \tag{42}$$

completes the derivation and yields

$$V = \frac{2k_1k_0}{k_1^4 - k_0^4}\left\{\frac{k_1}{k_0}\frac{\exp(-jk_1\rho)}{\rho} - \frac{k_0}{k_1}\frac{\exp(-jk_0\rho)}{\rho} - \frac{\pi}{2}\xi_{\text{pole}}\left[H_0^{(1)}\left(k_1/k_0, \xi_{\text{pole}}\rho\right) - H_0^{(1)}\left(k_0/k_1, \xi_{\text{pole}}\rho\right)\right]\right\} + \int_0^\infty \frac{2\{\exp[-l(z+h)] - 1\}}{lk_1^2 + mk_0^2} J_0(\xi\rho)\xi\, d\xi, \tag{43}$$

where the positive form of equation (31) is used for ξ_{pole}. Values for incomplete Hankel functions may be attained via numerical expansion. For completeness the useful relation

$$W = -\frac{\partial}{\partial z}\left[2G_1 - \left(k_0^2 + k_1^2\right)V\right] \tag{44}$$

expresses the last Sommerfeld integral W in terms of V.

[41] The leading terms of equations (40) and (43) show evidence of a pseudolateral wave, which originates in the less dense media and propagates along the surface (inside the dielectric). This phenomenon resembles the lateral wave that has application in geophysical exploration of the lithosphere [*King et al.*, 1986] and propagation modeling in highly vegetated environments [*Li et al.*, 1998]. Lateral waves are excited along a boundary between two media by a source either at the interface or in the dense medium and travel atop the interface in the less dense medium. Lateral and pseudolateral waves are illustrated in Figure 10.

[42] To highlight the surface and pseudolateral waves near the surface, field strength and GO error were

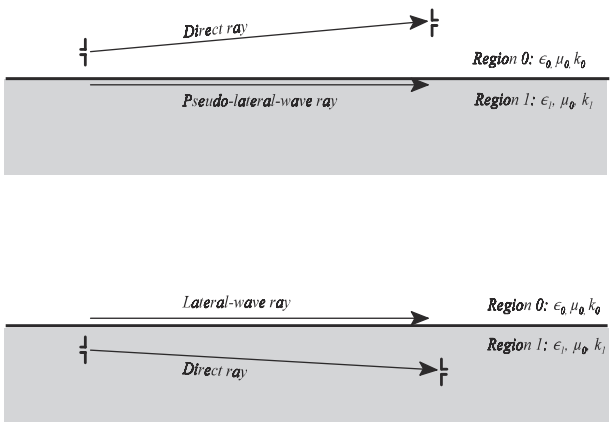

Figure 10. Pseudolateral versus lateral wave propagation scenarios.

assigned colors and plotted versus frequency and horizontal separation in Figure 11. It displays Sommerfeld solutions for copolarized fields (e.g., $|E_z^S|$ for VED), residual errors (e.g., $\| |E_z^S| - |E_z^{\mathrm{GO}}| \|$), and dashed curves representing the $R_0 = 10\lambda$ contour. For the chosen geometry (i.e., $h = z = 0.01$ m) the VED excites significant surface wave effects for frequencies approaching 5 GHz. Comparatively, HED-TE fields demonstrate weaker surface wave effects; hence the subtle oscillations due to the pseudolateral wave can be observed. In section 7, time domain results will also illustrate the pseudolateral wave with a pulse arrival time corresponding to wave velocity of the dense media.

5.2.3. Near-Field Effects on the Direct Ray

[43] Electromagnetic fields in the near-field region were computed via numerical evaluation of Sommerfeld integrals and compared to GO approximations in

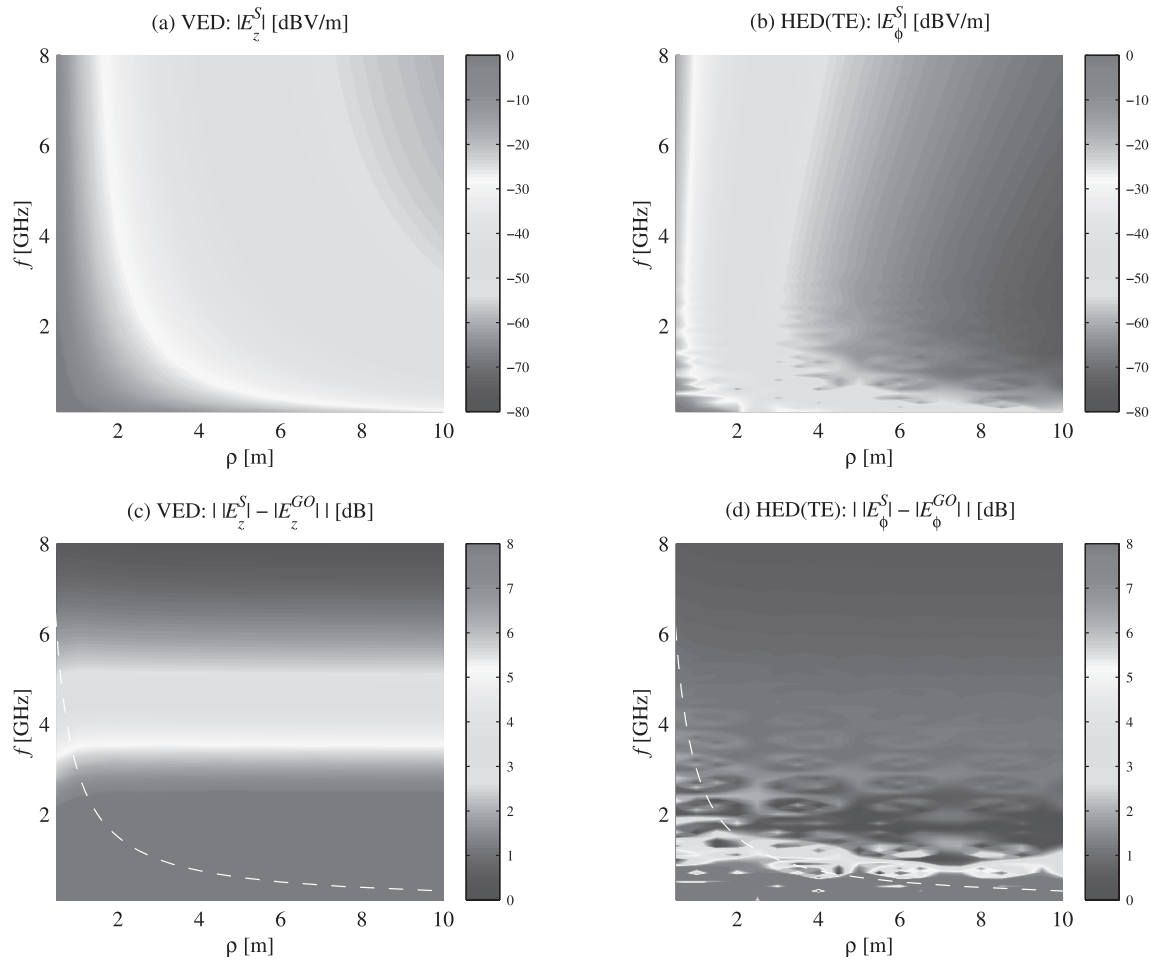

Figure 11. (a and b) Sommerfeld field strength and (c and d) GO residual error versus frequency and horizontal separation for a dipole above a concrete half-space ($h = z = 0.01$ m). Figures 11a and 11c show surface wave effects, and Figures 11b and 11d show pseudolateral wave effects. See color version of this figure at back of this issue.

Figures 5, 7, and 9. Note that Norton surface wave approximations are not included in these plots because they are valid only in the far-field region. As separation decreases to $\rho < \lambda$, the direct ray is observed in the near field of the source, and field components influenced by the direct ray (i.e., E_z and H_ϕ for VED and E_ϕ and H_z for HED-TE) demonstrate deviation from the GO approximation at low frequencies due to near-field effects. At $h = z = 10$ m the reflected ray travels well into the far field of the source before being reflected and observed; consequently, field components influenced by the reflected ray and not the direct ray (i.e., E_ρ for VED, H_ρ for HED-TE, and E_z and H_ϕ for HED-TM) show little near-field error.

[44] In Figures 8 and 9 the E_ρ component of the HED-TM radiated field displays an oscillatory deviation from the GO plus Norton term approximation when locations are many wavelengths from the interface and from each other. The general expressions for fields of the direct ray in spherical coordinates are

$$E_r = \frac{p}{2\pi R_0^2}\sqrt{\frac{\mu_0}{\epsilon_0}}\cos\theta_d\left[1+\frac{1}{jk_0R_0}\right]\exp(-jk_0R_0),$$

$$E_\theta = \frac{jk_0p}{4\pi R_0}\sqrt{\frac{\mu_0}{\epsilon_0}}\sin\theta_d\left[1+\frac{1}{jk_0R_0}-\frac{1}{(k_0R_0)^2}\right]\exp(-jk_0R_0),$$

$$H_\phi = \frac{jp}{4\pi R_0}\sin\theta_d\left[1+\frac{1}{jk_0R_0}\right]\exp(-jk_0R_0). \quad (45)$$

Notice that E_r is strictly a near- and intermediate-field expression with an $\exp(-jk_0R_0)$ phase dependence that is not accounted for in the geometric optics expressions. For the HED-TM case, if $\theta_d = 0°$, then E_r is equivalent to the direct ray of E_ρ in equation (22) and near-field influence is maximized in the null of the antenna pattern because the $\cos\theta_d$ factor is equal to 1. The oscillatory deviation, mentioned at the top of the paragraph, occurs because the near-field direct ray is comparable in magnitude to the reflected ray. Further discussion is given section 7, where the event is more intuitive.

6. Time Domain Analysis

[45] Field strength plots in the frequency domain are descriptive, but the practical significance of the results can be difficult to interpret. Of more importance to the digital communications engineer is how the errors translate to the time domain. In order to assess the practical significance of GO error for indoor scenarios we compute the delay spread of the channel impulse response. This section provides a detailed explanation of the time domain analyses used in this article.

[46] Digital signals are typically transmitted by some type of carrier modulation. The transmitted signal is limited in bandwidth to an interval of frequencies centered around the carrier or center frequency (i.e., $\omega_c = 2\pi f_c$) and must be real-valued in the time domain in order to have a physical interpretation; consequently, it is complex-conjugate symmetric about DC in the frequency domain. For mathematical convenience with no loss in generality the passband signal may be expressed as a complex-baseband representation. This is accomplished by first filtering out the negative frequencies to produce an analytic signal and then shifting the analytic signal down to baseband. In the time domain the real and imaginary parts of the analytic signal are a Hilbert transform pair. A pictorial representation of real-time, analytic, and complex-baseband signals is given in Figure 12, and more extensive discussions are given by *Bedrosian* [1962] and *Vakman* [1998].

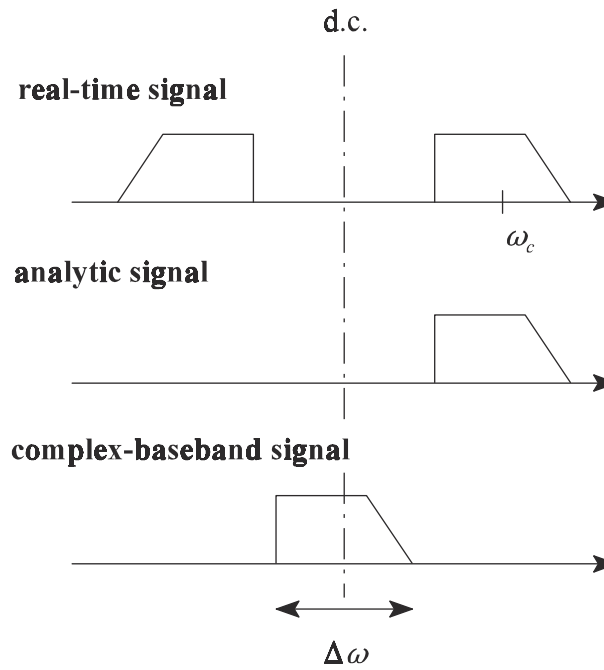

Figure 12. Signal representations.

[47] We seek an expression for the magnitude of the impulse response $|g(t, \tau)|$ in terms of electric and magnetic field variables in order to compute delay spread via equations (2) and (3). The impulse response of the channel can be given by

$$g(t,\tau) = \mathbf{v}\cdot\begin{cases}\mathbf{e}(t,\tau),\\ \mathbf{h}(t,\tau),\end{cases} \quad (46)$$

where $\mathbf{v}$ is a unit direction vector corresponding to the receive antenna. The complex-baseband representation

of the applicable vector field components, $\mathbf{e}(t, \tau)$ and $\mathbf{h}(t, \tau)$, is given by

$$\mathbf{e}(t,\tau) = \mathrm{FT}^{-1}[\mathbf{E}(t,\omega+\omega_c)\Lambda(\omega+\omega_c)],$$
$$\mathbf{h}(t,\tau) = \mathrm{FT}^{-1}[\mathbf{H}(t,\omega+\omega_c)\Lambda(\omega+\omega_c)], \quad (47)$$

where FT^{-1} is the inverse Fourier transform operator, τ is the transform variable, and $\Lambda(\omega)$ is a scalar window function that filters out negative frequencies and defines the pulse shape of the signal. For this study a Hamming window was used for $\Lambda(\omega)$. Note that band limiting the signal introduces artifacts into the analysis (e.g., finite pulse width and sidelobes associated with the window shape).

7. Time Domain Results

[48] Impulse responses for an ultrawideband (i.e., BW = 660 MHz) signal centered at 900 MHz (i.e., λ_c = 0.33 m) are given in Figures 13–18; the eight geometries are the same as those used in the frequency domain analysis. The astute reader will justifiably balk at the idea of a 900-MHz dipole with a 73% emission bandwidth. Keep in mind, however, that this is an analytical investigation where decisions are made to focus on fundamental electromagnetic behavior. The wide bandwidth was chosen to enhance the near-surface and near-field effects for identification purposes. Delay spread was calculated for each impulse response in order to quantify discrepancies between the different models.

7.1. Near-Surface Effects

[49] Near-surface effects are best observed at $h = z$ = 0.01 m in Figures 13, 15, and 17. The blue curve (i.e., GO plus Norton term) isolates surface wave effects. In the frequency domain the surface wave causes an increase in field strength concentrated at DC; in the time domain this corresponds to time-dispersed energy, which raises the pulse sidelobes. Also, the surface wave has an $\exp(-jk_0R_1)$ phase dependence; hence an additional surface wave pulse arrives at the same delay as the reflected ray.

[50] The green curve (i.e., Sommerfeld solution) demonstrates a delayed pulse near 37 ns due to the pseudolateral wave phenomenon. A wave propagating 5 m through concrete at $(\epsilon\mu_0)^{-1/2} \approx 1.34 \times 10^8$ m/s arrives at the observation point with a 37.4 ns delay; this statement supports the mathematical pseudolateral wave description in section 5.2.

[51] Figure 19 illustrates delay spread (from the Sommerfeld solution) and percentage delay spread error (associated with the GO approximation) as a function of bandwidth and center frequency for scenarios identical to those in Figure 11 restricted to ρ = 5 m. Notice that although the pseudolateral wave (from HED-TM excitation) was relatively weaker than the surface wave (from VED excitation), it can have a more significant effect on delay spread.

7.2. Near-Field Effects

[52] As shown in Figures 14, 16, and 18, the reactive nature of the near field dominates for $\rho \leq 0.1$ m. This is expected, as the separation is well within a carrier wavelength. When the direct ray is observed in the near field, GO error increases because the near-field direct-pulse energy is dispersed over time.

[53] As discussed in section 5.2.3, an interesting event occurs when the observation point lies directly in the null of the x-aligned antenna pattern (see HED-TM results in Figures 17 and 18). The transverse field components (i.e., e_z and h_ϕ) corresponding to the direct pulse are attenuated because of the orientation of the dipole. The radial component (i.e., e_ρ) corresponding to the direct ray, however, is influential because of near- and intermediate-field propagation. For this case the presence of the near-field direct ray causes unacceptable error in the GO delay spread approximation.

8. Conclusion

[54] In this article, the error associated with GO predictions for indoor propagation models was evaluated. Our conclusions were based on results from the classical problem of infinitesimal dipoles above a lossy half-space. Exact (i.e., Sommerfeld) and approximate (i.e., GO and GO plus Norton surface wave term) formulations for infinitesimal dipole sources were summarized, and numerical schemes for evaluating the complex integrals in the Sommerfeld formulation were given. Eight canonical geometries were chosen to isolate individual propagation effects on relevant field components. Simulation scenarios were limited to the material properties of concrete and physical dimensions up to 10 m and as small as 1 cm. Results were given in both the frequency and time domains.

[55] As expected, GO predictions agreed with the numerical approximations to Sommerfeld integrals when the source and observation points were multiple wavelengths above the surface and multiple wavelengths apart. However, when the antennas were brought close to the surface and close together, classic surface wave and near-field effects were observed. An additional propagation mechanism we call the pseudolateral wave was identified.

[56] A summary of observations follows. The following surface wave observations were made: (1) Surface wave effects peak at DC and decrease sharply with increasing frequency; in the time domain this translates

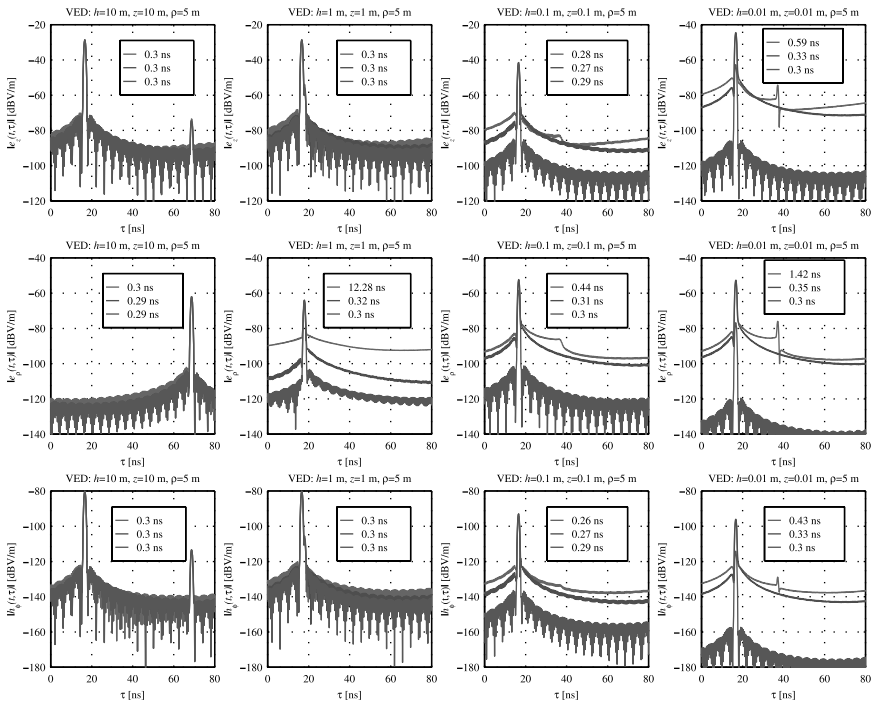

Figure 13. Near-surface effects on impulse responses of a VED above a concrete half-space. Legends display Sommerfeld (green), GO plus Norton term (blue), and GO (red) estimates to delay spread. See color version of this figure at back of this issue.

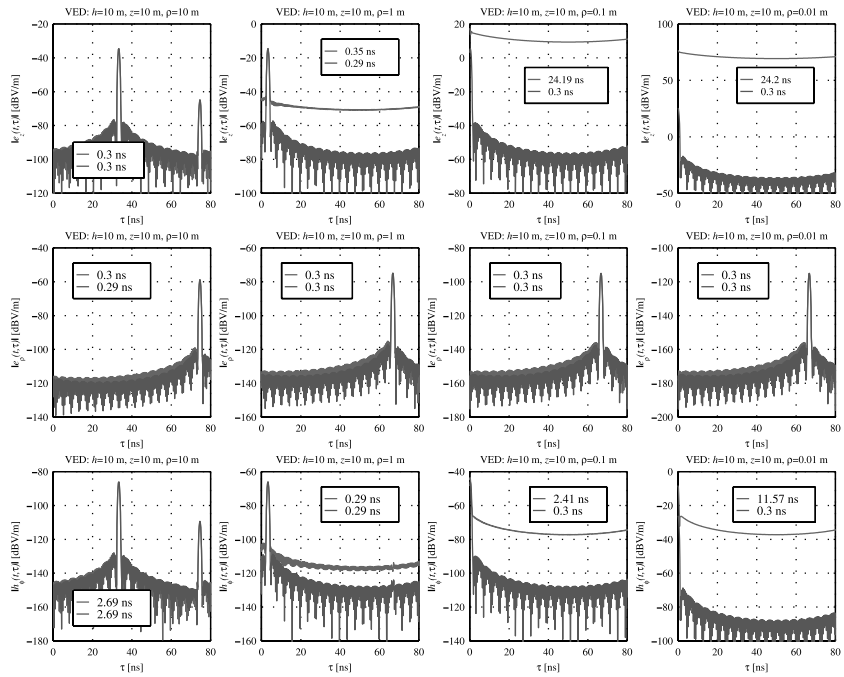

Figure 14. Near-field effects on impulse responses of a VED above a concrete half-space. Legends display Sommerfeld (green) and GO (red) estimates to delay spread. See color version of this figure at back of this issue.

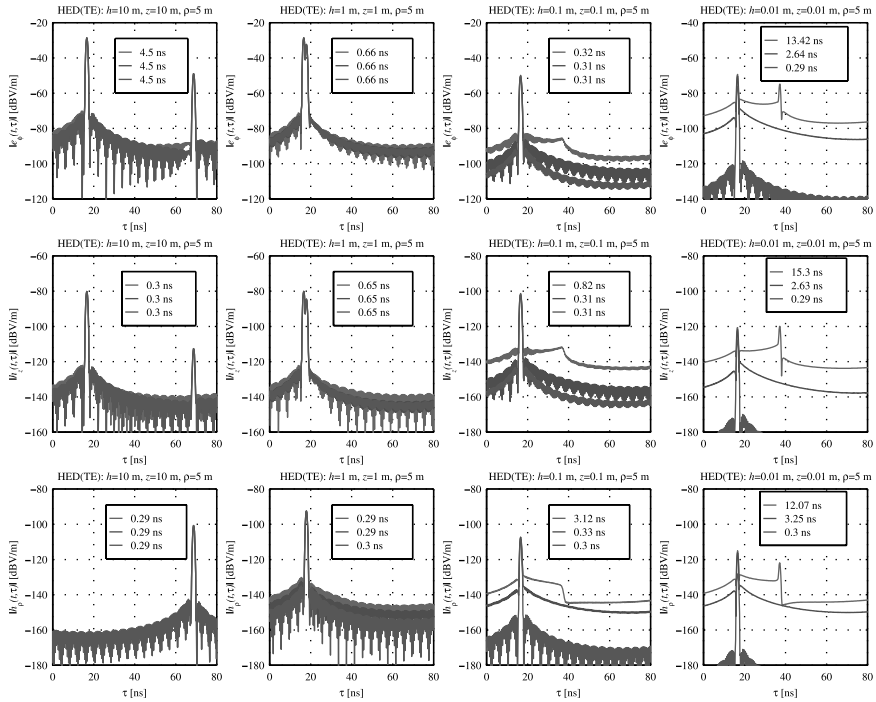

Figure 15. Near-surface effects on impulse responses of an *x*-aligned HED (TE, $\phi = 90°$) above a concrete half-space. Legends display Sommerfeld (green), GO plus Norton term (blue), and GO (red) estimates to delay spread. See color version of this figure at back of this issue.

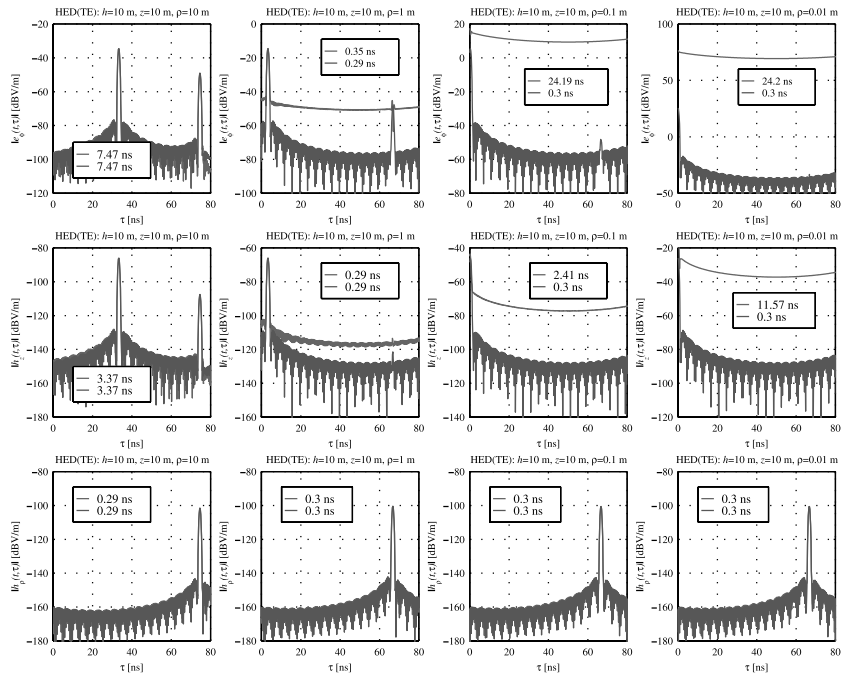

Figure 16. Near-field effects on impulse responses of an *x*-aligned HED (TE, $\phi = 90°$) above a concrete half-space. Legends display Sommerfeld (green) and GO (red) estimates to delay spread. See color version of this figure at back of this issue.

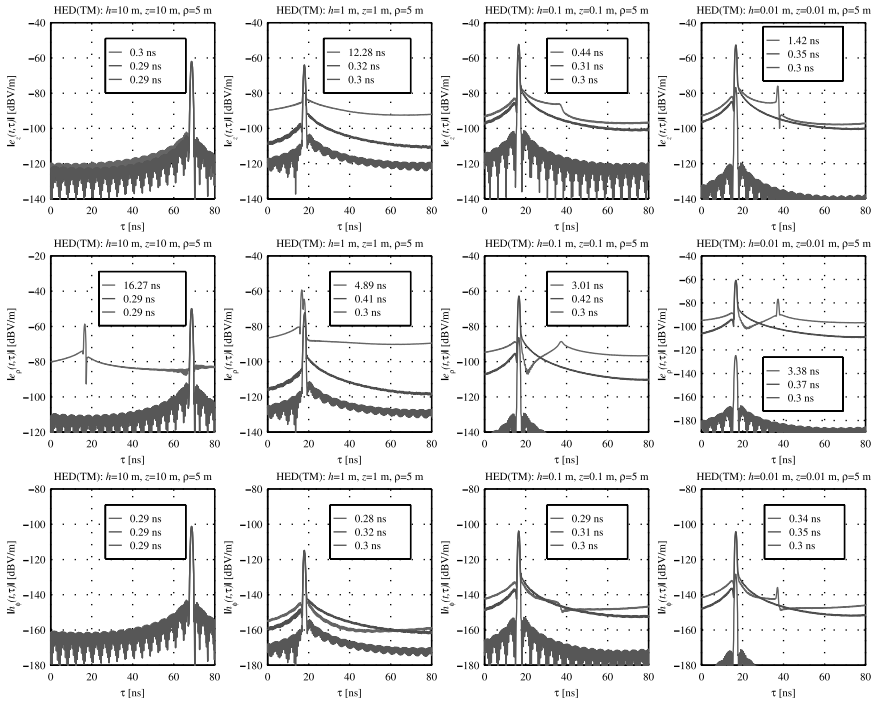

Figure 17. Near-surface effects on impulse responses of an *x*-aligned HED (TM, $\phi = 0°$) above a concrete half-space. Legends display Sommerfeld (green), GO plus Norton term (blue), and GO (red) estimates to delay spread. See color version of this figure at back of this issue.

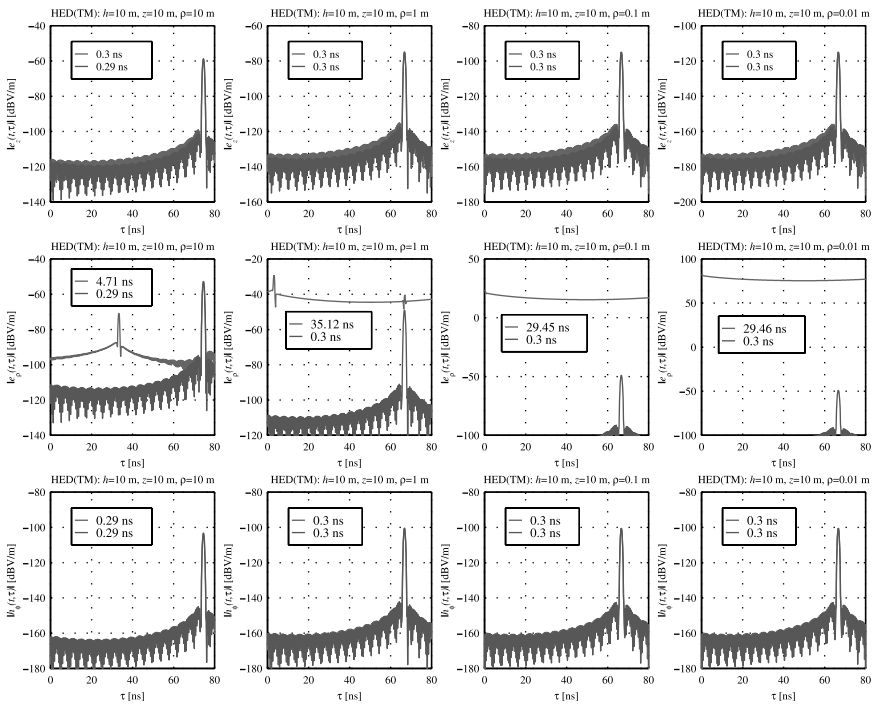

Figure 18. Near-field effects on impulse responses of an *x*-aligned HED (TM, $\phi = 0°$) above a concrete half-space. Legends display Sommerfeld (green) and GO (red) estimates to delay spread. See color version of this figure at back of this issue.

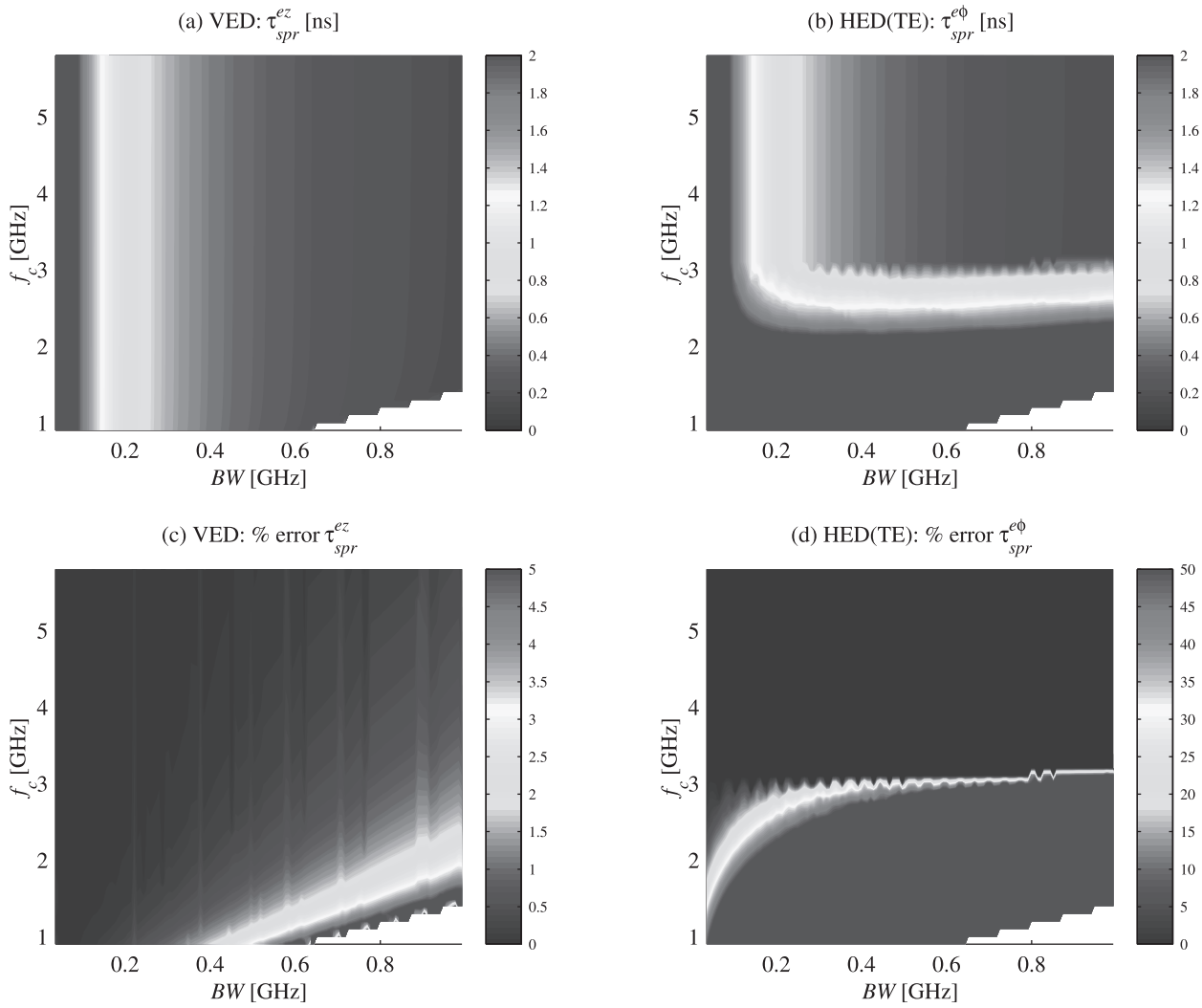

Figure 19. (a and b) Delay spread and (c and d) percent error versus bandwidth and center frequency for dipoles above a concrete half-space ($h = z = 0.01$ m, $\rho = 5$ m). Figures 19a and 19c show surface wave effects, and Figures 19b and 19d show pseudolateral wave effects. See color version of this figure at back of this issue.

to time-dispersed energy. (2) Surface waves also have a $\exp(-jk_0R_1)$ phase dependency that arrives at the reflected-ray delay. (3) Surface wave propagation is more influential in VED and HED-TM fields than in HED-TE fields.

[57] The following pseudolateral wave observations were made: (1) Pseudolateral waves propagate inside the lossy medium at the corresponding wave velocity. (2) Pseudolateral wave propagation is more influential under weak surface wave conditions. (3) Observed pseudolateral waves were weaker than surface waves but can cause more significant effects on delay spread.

[58] The following near-field observations were made: (1) Near-field effects peak at DC and decrease sharply with increasing frequency; this corresponds to dispersing the energy in the time domain. (2) Near-field error depends on the individual propagation paths and field components. (3) Near-field effects are significant for radial fields observed in the null of the dipole antenna pattern at observation points many wavelengths away.

[59] Conditions which cause the GO approximation to be invalid were demonstrated; these conditions depend on the antenna types and position, the material composition of the reflecting surface, the operational frequency band, etc. General expressions for infinitesimal electric dipoles above a half-space have been provided to improve the accuracy of GO predictions by accounting for surface wave and near-field effects. More specifically, the GO

approximation may be complemented by the Norton surface wave terms in equations (18), (21), and (22) and by the near-field terms in equation (45) to model the direct ray. These expressions, however, apply only to infinitesimal dipoles above a dielectric half-space. Care should be taken when modeling actual antennas and finite-thick reflection surfaces.

[60] As demonstrated, pseudolateral wave effects can be severe. The leading terms of equations (40) and (43) show evidence of the pseudolateral wave; these equations, however, are cumbersome and require numerous derivatives and substitutions in order to acquire field equations. A more mathematically rigorous derivation is necessary in order to provide a closed-form asymptotic approximation to the pseudolateral wave.

[61] **Acknowledgments.** The authors thank George A. Hufford, J. Randy Hoffman, Paul McKenna, and Robert J. Achatz for insights shared.

References

Baños, A., *Dipole Radiation in the Presence of a Conducting Half-Space*, Pergamon, New York, 1966.

Bedrosian, E., The analytic signal representation of modulated waveforms, *Proc. IRE*, *50*, 2071–2076, 1962.

Bello, P. A., and B. D. Nelin, The effect of frequency selective fading on the binary error probabilities of incoherent and differentially coherent matched filter receivers, *IEEE Trans. Commun. Syst.*, *11*(2), 170–186, 1963.

Bronson, G., K. Pahlavan, and H. Rotithor, Performance prediction of wireless LANs based on ray tracing algorithms, paper presented at International Symposium on Personal, Indoor, and Mobile Radio Communication, Inst. of Electr. and Electron. Eng., Yokohama, Japan, Oct. 1993.

Burr, A. G., Modulation and multipath countermeasures, in *Modern Personal Radio Systems*, edited by R. C. V. Macario, pp. 43–78, Inst. of Electr. Eng., London, 1996.

Chen, S. H., and S. K. Jeng, An SBR/Image approach to indoor radio wave propagation in indoor environments with metallic furniture, *IEEE Trans. Antennas Propag.*, *45*(1), 98–106, 1997.

Chuang, J. C. I., The effects of time delay spread on portable radio communication channels with digital modulation, *IEEE J. Selected Areas Commun.*, *5*(5), 879–889, 1987.

Cotton, M. G., E. F. Kuester, and C. L. Holloway, A frequency- and time-domain investigation into the geometric optics approximation for wireless indoor applications, *NTIA Rep. 00-379*, Natl. Telecommun. and Inf. Admin., Boulder, Colo., June 2000.

Devasirvatham, D. M. J., Multipath time delay spread in the digital portable radio environment, *IEEE Commun. Mag.*, *25*(6), 13–21, 1987.

Durgin, G., N. Patwari, and T. S. Rappaport, Improved 3D ray launching method for wireless propagation prediction, *Electron. Lett.*, *33*(16), 1412–1413, 1997.

Greenstein, L. J., and V. K. Prabhu, Analysis of multipath outage with applications to 90-Mbits/s PSK systems at 6 and 11 GHz, *IEEE Trans. Commun.*, *27*(1), 68–75, 1979.

Halabe, U. H., A. Sotoodehnia, K. R. Maser, and E. A. Kausel, Modeling the electromagnetic properties of concrete, *ACI Mater. J.*, *90*(6), 552–563, 1993.

Holloway, C. L., M. G. Cotton, and P. McKenna, A model for predicting the power delay profile characteristics inside a room, *IEEE Trans. Veh. Technol.*, *48*(4), 1110–1120, 1999.

Holt, T., K. Pahlavan, and J. F. Lee, A graphical indoor radio channel simulator using ray tracing, paper presented at International Symposium on Personal, Indoor, and Mobile Radio Communication, Inst. of Electr. and Electron. Eng., Boston, Mass., Oct. 1992.

Honcharenko, W., H. L. Bertoni, J. L. Dailing, J. Qian, and H. D. Yee, Mechanisms governing UHF propagation on single floors in modern office buildings, *IEEE Trans. Veh. Technol.*, *41*(4), 496–504, 1992.

Jakes, W. C., An approximate method to estimate an upper bound on the effect of multipath delay distortion on digital transmission, *IEEE Trans. Commun.*, *27*(1), 76–81, 1979.

Johnk, C., *Engineering Electromagnetic Fields and Waves*, John Wiley, New York, 1988.

Johnson, W. A., and D. G. Dudley, Real axis integration of Sommerfeld integrals: Source and observation points in air, *Radio Sci.*, *18*(2), 175–186, 1983.

King, R. W., M. Owens, and T. T. Wu, Properties of lateral electromagnetic fields and their application, *Radio Sci.*, *21*(1), 13–23, 1986.

Kuester, E. F., and D. C. Chang, Evaluation of Sommerfeld integrals associated with dipole sources above Earth, *Sci. Rep.43*, Univ. of Colo., Boulder, Jan. 1979.

Kunz, K. S., and R. J. Luebbers, *The Finite Difference Time Domain Method for Electromagnetics*, CRC Press, Boca Raton Fla., 1993.

Kürner, T., D. J. Cichon, and W. Wiesbeck, Evaluation and verification of the VHF/UHF propagation channel based on a 3-D-wave propagation model, *IEEE Trans. Antennas Propag.*, *43*(4), 879–891, 1994.

LaMaire, R. O., A. Krishna, P. Bhagwat, and J. Panian, Wireless LANs and mobile networking standards and future directions, *IEEE Commun. Mag.*, *34*(8), 86–94, 1996.

Lauer, A., I. Wolff, A. Bahr, J. Pamp, J. Kunisch, and I. Wolff, Multi-mode FDTD simulations of indoor propagation including antenna properties, paper presented at Vehicular Technology Conference, Inst. of Electr. and Electron. Eng., Chicago, Ill., July 1995.

Lawton, M. C., and J. P. McGeehan, The application of GTD and ray launching to channel modeling for cordless radio systems, paper presented at Vehicular Technology Conference, Inst. of Electr. and Electron. Eng., Denver, Colo., May 1992.

Lawton, M. C., and J. P. McGeehan, The application of a deterministic ray launching algorithm for the prediction of

radio channel characteristics in small-cell environments, *IEEE Trans. Veh. Technol.*, *43*(4), 955–968, 1994.

Li, L. W., T. S. Yeo, P. S. Kooi, and M. S. Leong, Radio wave propagation along mixed paths through a four-layered model of rain forest: An analytic approach, *IEEE Trans. Antennas Propag.*, *46*(7), 1098–1111, 1998.

Lytle, R. J., and D. L. Lager, Numerical evaluation of Sommerfeld integrals, *Rep. W-7405-Eng-48*, Lawrence Livermore Natl. Lab., Livermore, Calif., Oct. 1974.

Maclean, T. S. M., and Z. Wu, *Radiowave Propagation Over Ground*, pp. 1–119, Chapman and Hall, New York, 1993.

Michalski, K. A., Extrapolation methods for Sommerfeld integral tails, *IEEE Trans. Antennas Propag.*, *46*, 1405–1418, 1998.

Mosig, J. R., Integral equation technique, in *Numerical Techniques for Microwave and Millimeter-Wave Passive Structures*, edited by T. Itoh, pp. 133–213, John Wiley, New York, 1989.

Norton, K. A., The propagation of radio waves over the surface of the earth and in the upper atmosphere, *Proc. IRE*, *25*(9), 1203–1236, 1937.

Press, W. H, B. P. Flannery, S. A. Teukolsky, and W. T. Vetterling, Integration of functions, in *Numerical Recipes*, pp. 102–130, Cambridge Univ. Press, New York, 1986.

Rappaport, T. S., and D. A. Hawbaker, A ray tracing technique to predict path loss and delay spread inside buildings, paper presented at GLOBECOM '92, Inst. of Electr. and Electron. Eng., Orlando, Fla., Dec. 1992.

Schauback, K. R., N. J. Davis, and T. S. Rappaport, A ray tracing method for predicting path loss and delay in microcellular environments, paper presented at Vehicular Technology Conference, Inst. of Electr. and Electron. Eng., Denver, Colo., May 1992.

Seidel, S. Y., and T. S. Rappaport, A ray tracing technique to predict path loss and delay spread inside buildings, paper presented at GLOBECOM '92, Inst. of Electr. and Electron. Eng., Orlando, Fla., Dec. 1992.

Seidel, S. Y., and T. S. Rappaport, Site-specific propagation prediction for wireless in-building personal communication system design, *IEEE Trans. Veh. Technol.*, *43*(4), 879–891, 1994.

Siller, C. A., Multipath propagation, *IEEE Commun. Mag.*, *22*(2), 6–15, 1984.

Sommerfeld, A., *Partial Differential Equations in Physics*, Academic, San Diego, Calif., 1964.

Taflove, A., *Computational Electrodynamics: The Finite-Difference Time-Domain Method*, Artech House, Norwood, Mass., 1995.

Talbi, L., and G. Y. Delisle, Finite difference time domain characterization of indoor radio propagation, in *Electromagnetic Waves, Prog. Electromagn. Res.*, vol. 12, edited by J. A. Kong, pp. 251–275, EMW, Cambridge, Mass., 1996.

Torres, R. P., L. Valle, M. Domingo, S. Loredo, and M. C. Diez, Cindoor: An engineering tool for planning and design of wireless systems in enclosed spaces, *IEEE Antennas Propag. Mag.*, *41*(4), 11–22, 1999.

Tyras, G., *Radiation and Propagation of Electromagnetic Waves*, Academic, San Diego, Calif., 1969.

Vakman, D., *Signals, Oscillations, and Waves: A Modern Approach*, Artech House, Norwood, Mass., 1998.

Valenzuela, R. A., A ray tracing approach to predicting indoor wireless transmission, paper presented at Vehicular Technology Conference, Inst. of Electr. and Electron. Eng., Secaucus, N. J., May 1993.

van der Pol, B., Theory of the reflection of the light from a point source by a finitely conducting flat mirror, with an application to radiotelegraphy, *Physica*, *2*, 843–853, 1935.

Wait, J. R., The ancient and modern history of EM groundwave propagation, *IEEE Antennas Propag. Mag.*, *40*(5), 7–24, 1998.

Wittmann, M., J. Marti, and T. Kurner, Impact of the power delay profile shape on the bit error rate in mobile radio systems, *IEEE Trans. Veh. Technol.*, *46*(2), 329–339, 1997.

Yang, G., K. Pahlavan, and J. F. Lee, A 3D propagation model with polarization characteristics in indoor radio channels, paper presented at GLOBECOM '93, Inst. of Electr. and Electron. Eng., Houston, Tex., Nov. 1993.

M. G. Cotton, Institute for Telecommunication Sciences, National Telecommunications and Information Administration, U.S. Department of Commerce, 325 Broadway, Boulder, CO 80305, USA. (mcotton@its.bldrdoc.gov)

C. L. Holloway, National Institute of Standards and Technology, U.S. Department of Commerce, Mail Code 813.02, 325 Broadway, Boulder, CO 80305-3328, USA. (holloway@boulder.nist.gov)

E. F. Kuester, Department of Electrical and Computer Engineering, University of Colorado, Campus Box 425, Boulder, CO 80309, USA. (kuester@schof.colorado.edu)

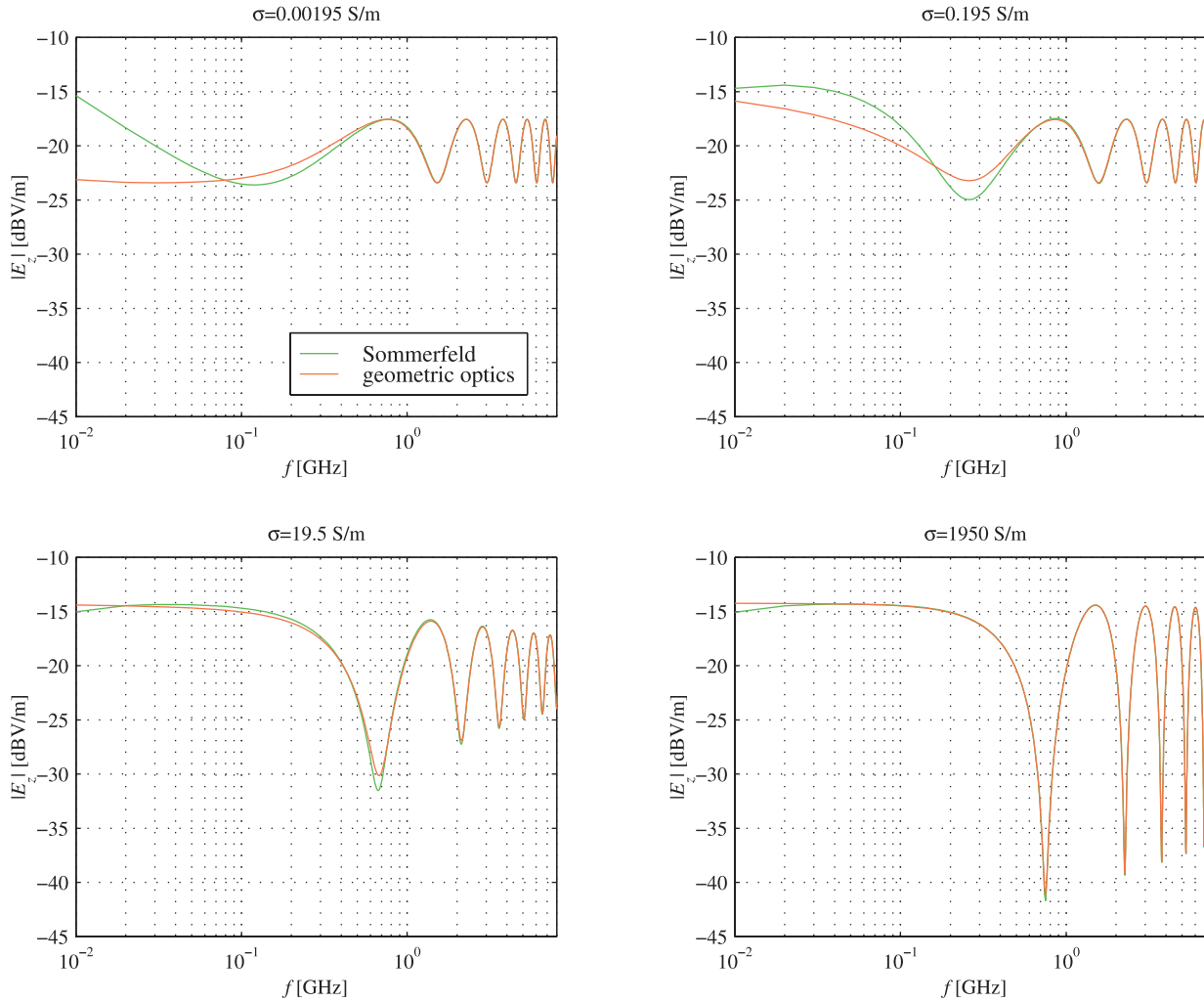

Figure 3. Electric field strength (z component) for a VED above a half-space ($z = h = 1$ m, $\rho = 10$ m, $\epsilon_r = 5$) at various conductivities.

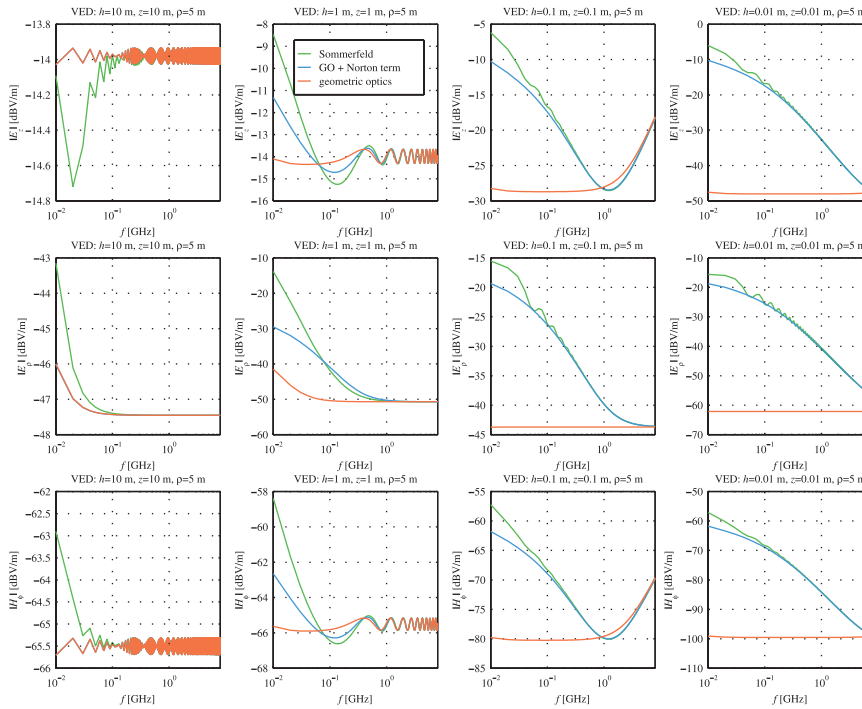

Figure 4. Near-surface effects on field strength of a VED above a concrete half-space.

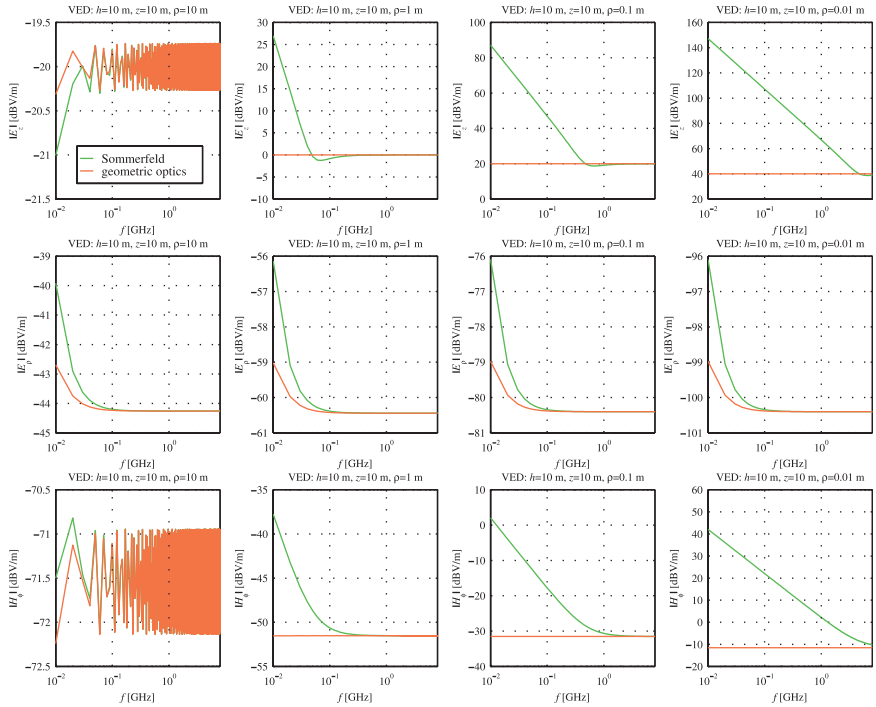

Figure 5. Near-field effects on field strength of a VED above a concrete half-space.

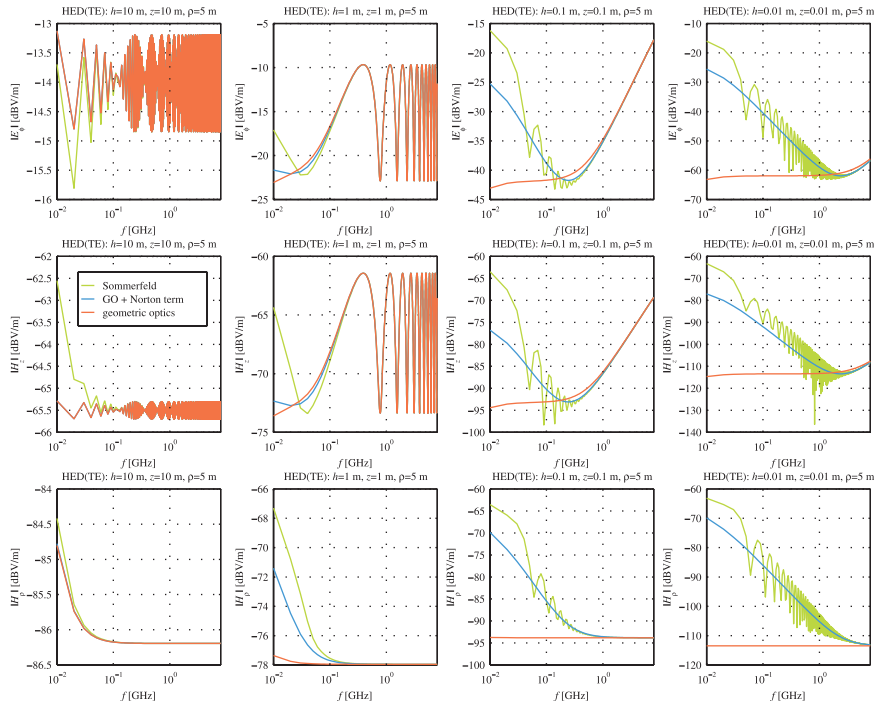

Figure 6. Near-surface effects on TE field strength of an *x*-aligned HED above a concrete half-space. Observation points are restricted to $\phi = 90°$.

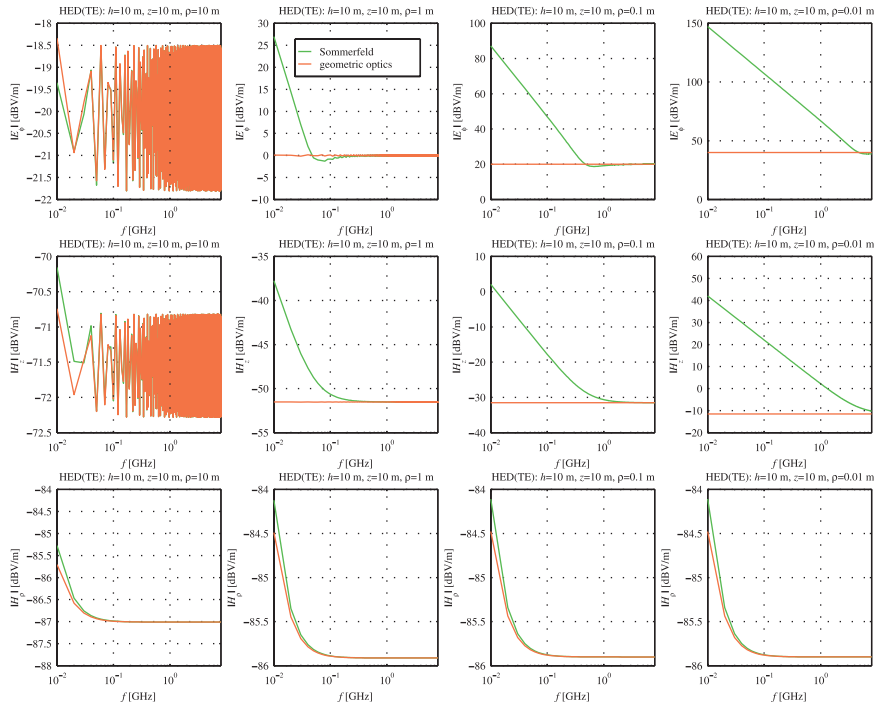

Figure 7. Near-field effects on TE field strength of an *x*-aligned HED above a concrete half-space. Observation points are restricted to $\phi = 90°$.

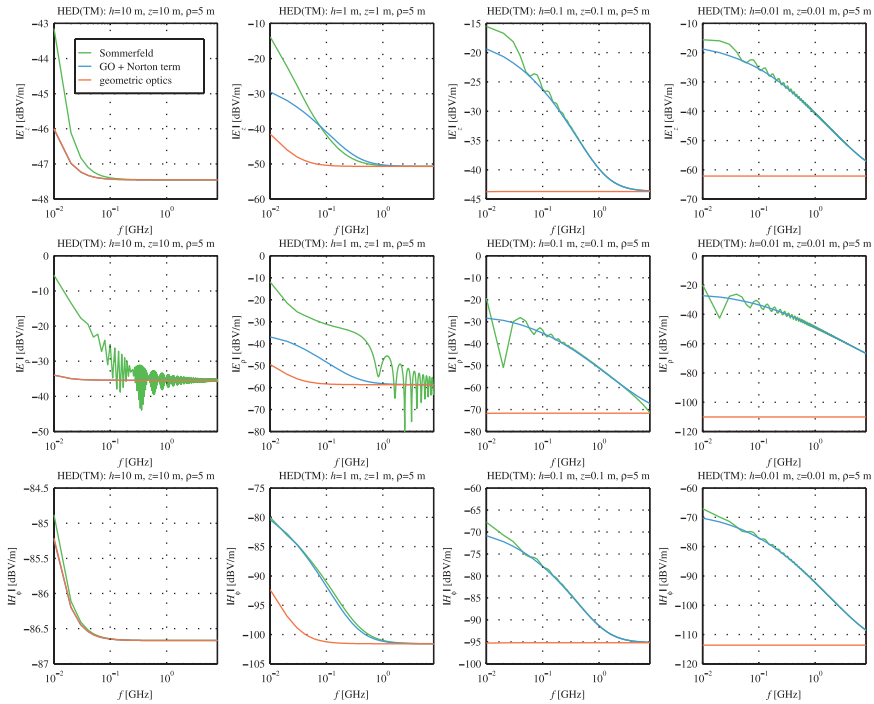

Figure 8. Near-surface effects on TM field strength of an *x*-aligned HED above a concrete half-space. Observation points are restricted to $\phi = 0°$.

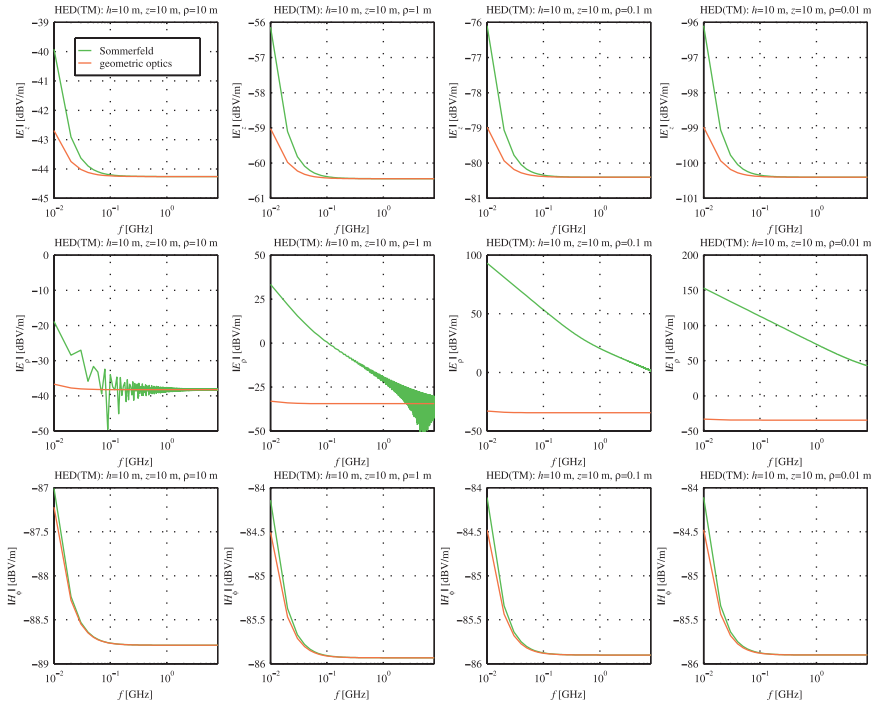

Figure 9. Near-field effects on TM field strength of an *x*-aligned HED above a concrete half-space. Observation points are restricted to $\phi = 0°$.

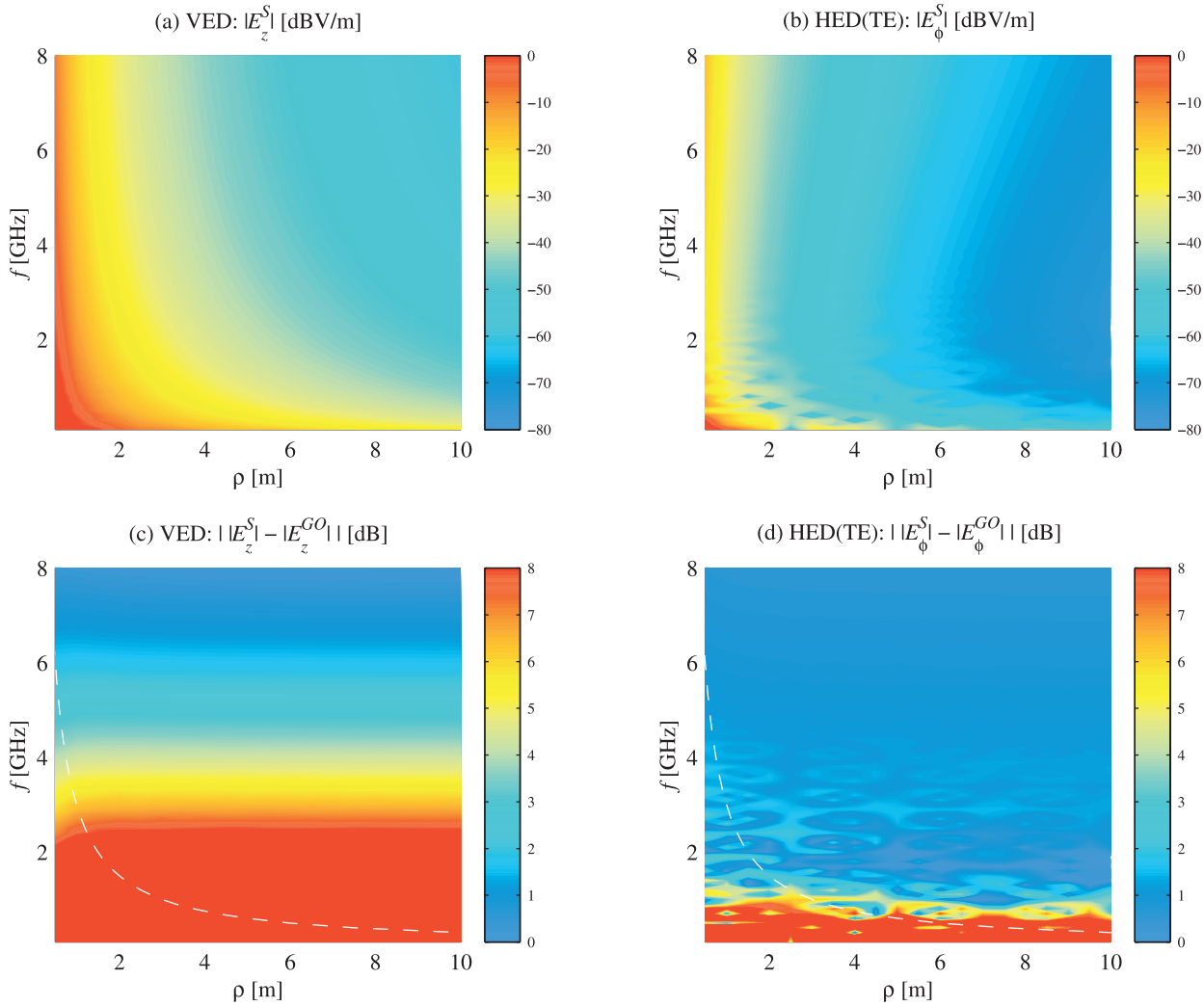

Figure 11. (a and b) Sommerfeld field strength and (c and d) GO residual error versus frequency and horizontal separation for a dipole above a concrete half-space ($h = z = 0.01$ m). Figures 11a and 11c show surface wave effects, and Figures 11b and 11d show pseudolateral wave effects.

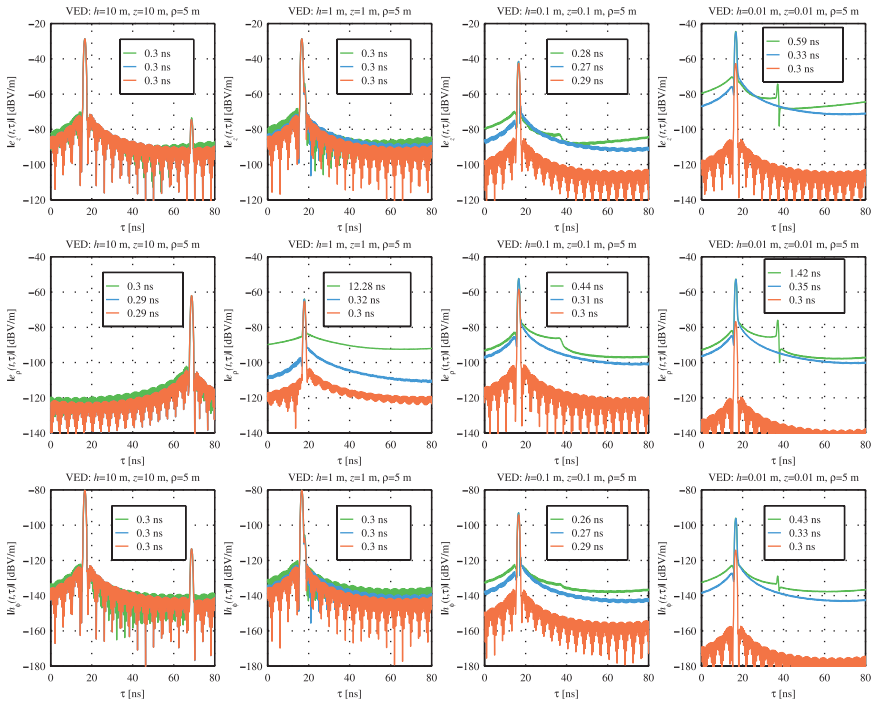

Figure 13. Near-surface effects on impulse responses of a VED above a concrete half-space. Legends display Sommerfeld (green), GO plus Norton term (blue), and GO (red) estimates to delay spread.

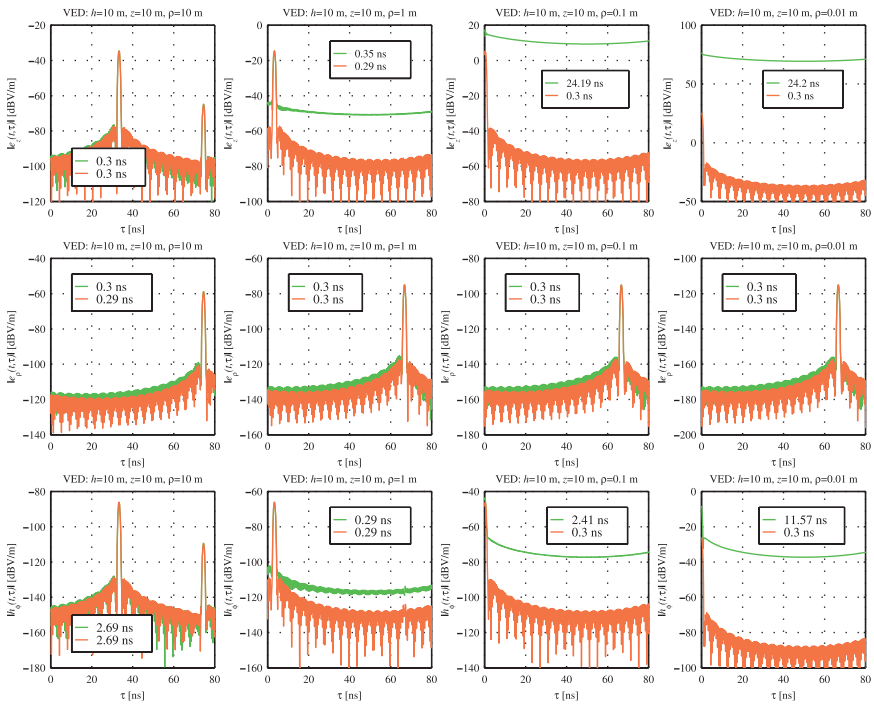

Figure 14. Near-field effects on impulse responses of a VED above a concrete half-space. Legends display Sommerfeld (green) and GO (red) estimates to delay spread.

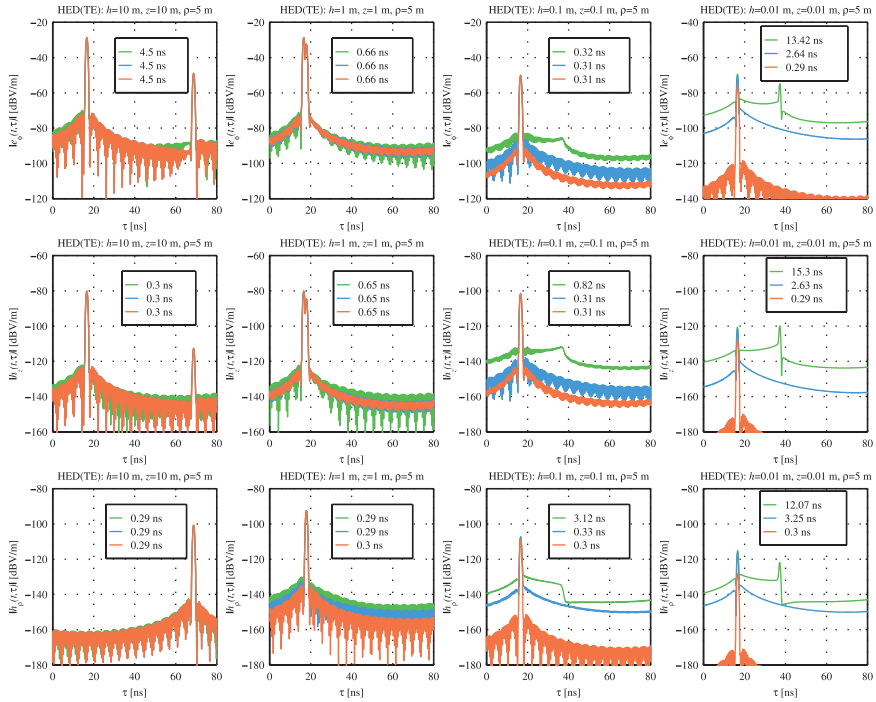

Figure 15. Near-surface effects on impulse responses of an *x*-aligned HED (TE, $\phi = 90°$) above a concrete half-space. Legends display Sommerfeld (green), GO plus Norton term (blue), and GO (red) estimates to delay spread.

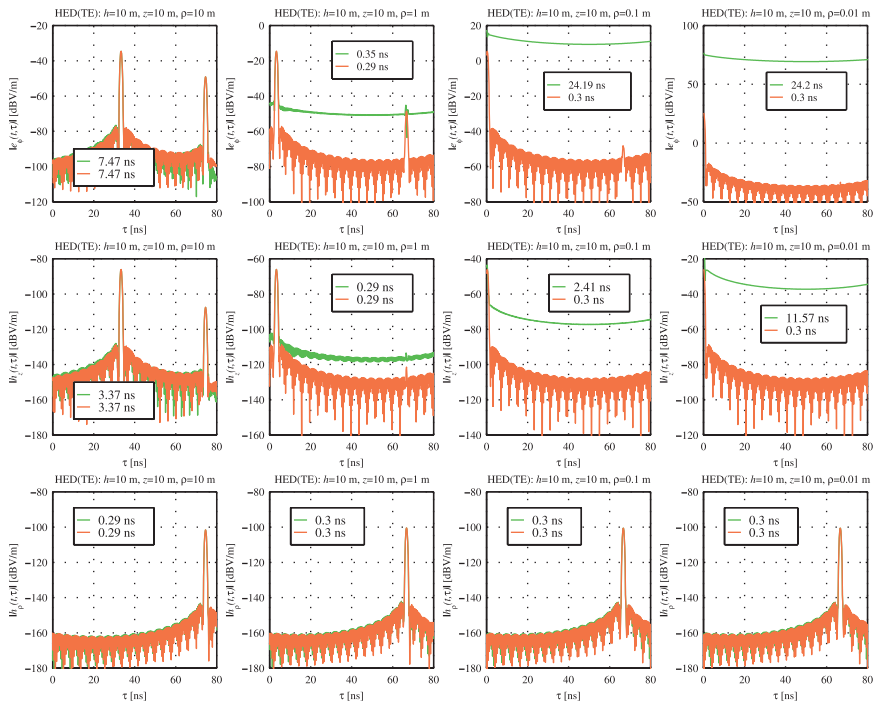

Figure 16. Near-field effects on impulse responses of an *x*-aligned HED (TE, $\phi = 90°$) above a concrete half-space. Legends display Sommerfeld (green) and GO (red) estimates to delay spread.

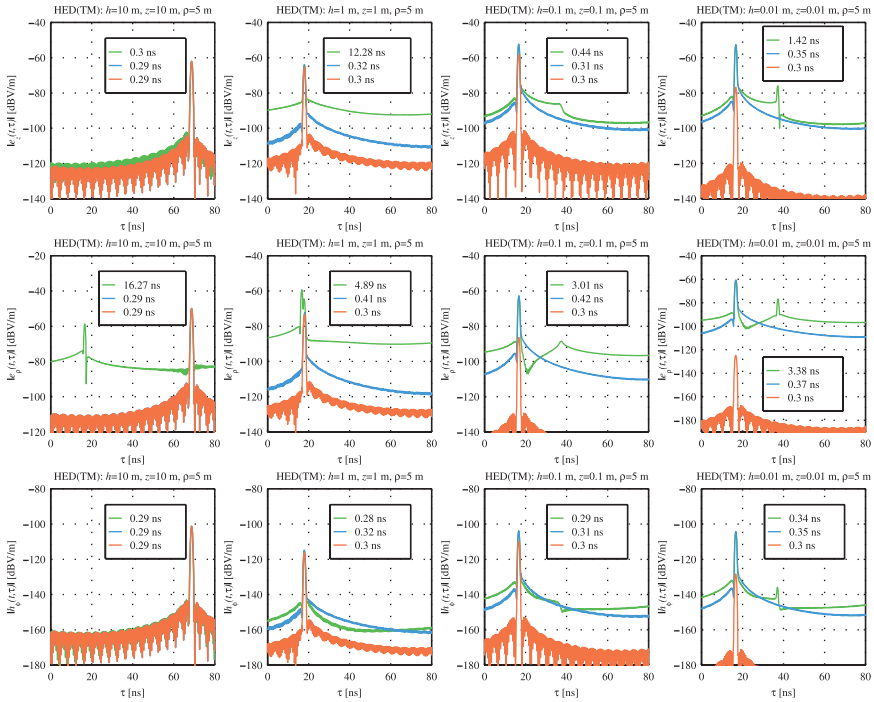

Figure 17. Near-surface effects on impulse responses of an *x*-aligned HED (TM, $\phi = 0°$) above a concrete half-space. Legends display Sommerfeld (green), GO plus Norton term (blue), and GO (red) estimates to delay spread.

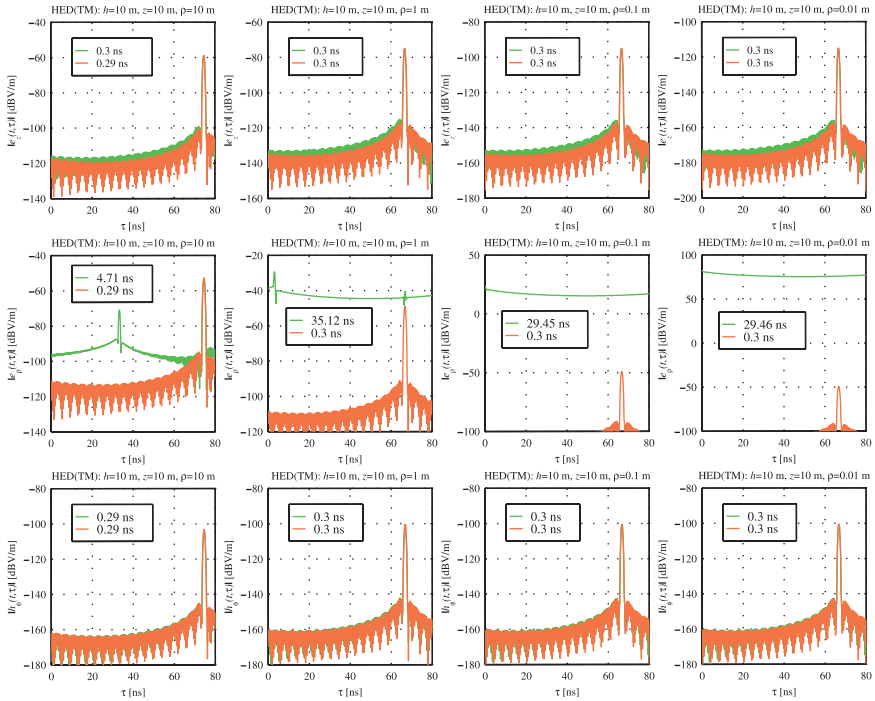

Figure 18. Near-field effects on impulse responses of an *x*-aligned HED (TM, $\phi = 0°$) above a concrete half-space. Legends display Sommerfeld (green) and GO (red) estimates to delay spread.

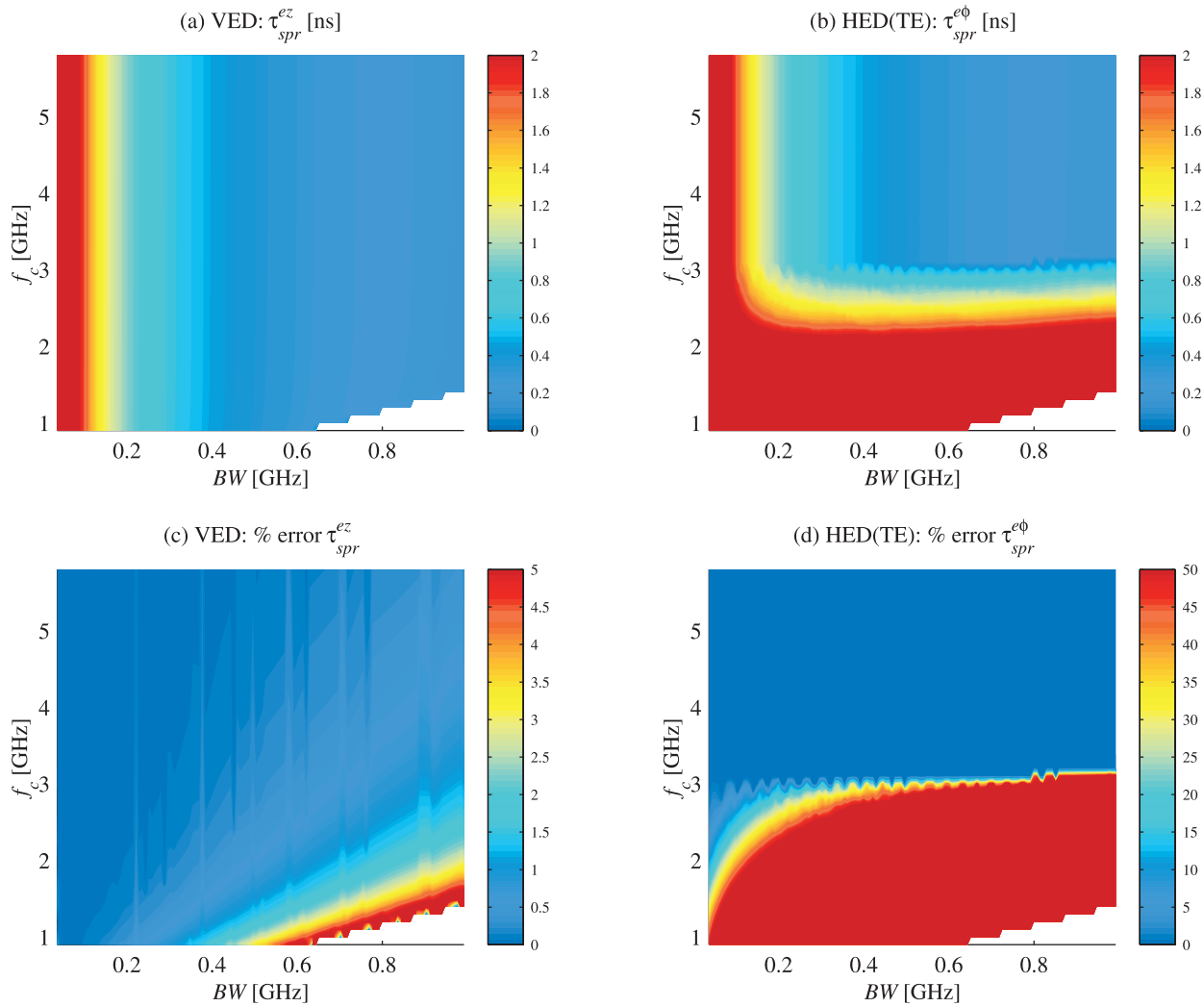

Figure 19. (a and b) Delay spread and (c and d) percent error versus bandwidth and center frequency for dipoles above a concrete half-space ($h = z = 0.01$ m, $\rho = 5$ m). Figures 19a and 19c show surface wave effects, and Figures 19b and 19d show pseudolateral wave effects.